Journal of Colloid and Interface Science 398 (2013) 193–209

Contents lists available at SciVerse ScienceDirect

Journal of Colloid and Interface Science

www.elsevier.com/locate/jcis

Low-frequency complex conductivity of sandy and clayey materials

A. Revil [a,b,*], J.D. Eppehimer [a], M. Skold [a], M. Karaoulis [a], L. Godinez [c], M. Prasad [c]

[a] Colorado School of Mines, Department of Geophysics, Golden, 80401 CO, USA
[b] ISTerre, UMR CNRS 5275, Université de Savoie, 73376 cedex, Le Bourget du Lac, France
[c] Colorado School of Mines, Department of Petroleum Engineering, Golden, 80401 CO, USA

ARTICLE INFO

Article history:
Received 29 November 2012
Accepted 6 January 2013
Available online 13 February 2013

Keywords:
Complexation
Electrical conductivity
Clay
Low-frequency dielectric spectroscopy
Quadrature conductivity
Cation exchange capacity
Specific surface area

ABSTRACT

Low-frequency polarization of sands and sandstones seems to be dominated by the polarization of the Stern layer, the inner part of the electrical double layer coating the surface of the silica grains and clay particles. We investigate a simple model of Stern layer polarization combined with a simple complexation model of the surface of the grains immersed in a 1:1 electrolyte like NaCl. In isothermal conditions, the resulting model can be used to predict the complex conductivity of clayey materials as a function of the porosity, the cation exchange capacity of the clay fraction (alternatively the specific surface area of the material), and the salinity of the pore water. A new set of experimental data is presented. This dataset comprises low-frequency (1 mHz–45 kHz) complex conductivity measurements of saprolites and sandstones that are well characterized in terms of their petrophysical properties (porosity, permeability, specific surface area or CEC, and pore size). This dataset, together with incorporating additional data from the literature, is used to test the Stern layer polarization model. We find an excellent agreement between the predictions of this model and this experimental dataset indicating that the new model can be used to predict the complex conductivity of natural clayey materials and clay-free silica sands.

1. Introduction

From non-equilibrium thermodynamics, the current density of a porous material can be written as the sum of the classical Ohm's law plus two source current densities, one associated with the gradient of the chemical potential of the charge carriers (diffusion current) and one with the pressure gradient (streaming current) [1–3]. These source current densities are responsible for a phase lag between the current and the electrical field for harmonic imposed current or electrical field [4–5]. The amplitude of the electrical conductivity and the phase can be used to define a complex electrical conductivity with an in-phase component characterizing electromigration and a quadrature component characterizing low-frequency polarization.

The understanding of the complex conductivity of dilute colloidal suspensions has been the subject of a high number of theoretical studies (e.g., [4,6]). The "standard" model developed by Dukhin and Shilov [4,7] is based on the polarization of the electrical diffuse layer. The standard model is, however, insufficient to reproduce the low-frequency polarization of colloidal suspensions [6]. It has been recognized back in the nineties that this deficiency could be explained by the polarization of the Stern layer and, since, a number of works have been devoted to understand the polarization of this layer [8,9].

Granular porous media are, however, not colloids because of their grain-to-grain contacts. As the grains are touching each other, there is an overlap of the diffuse layer in porous media from grain-to-grain. This overlapping may decrease the dipole moment associated with the polarization of the diffuse layer. The Stern layer remains, however, discontinuous. In a set of previous studies, Revil and co-workers have argued that the polarization of the Stern layer may be the dominant polarization mechanism in sandy and clayey porous materials [5,10–14].

In the present paper, following [12], we provide a simple polarization model of sands and clayey materials based on the polarization of the Stern layer neglecting completely the polarization of the diffuse layer. We also present a new set of experimental data on saprolites and sandstones. We see that the Stern layer polarization model seems to explain well these experimental data. It can be therefore used to develop time-lapse tomographic methods to visualize non-intrusively changes in the pore water chemistry and interfacial chemistry in granular media such as sands and clayey materials and using techniques developed in geophysical and medical imaging.

* Corresponding author at: Colorado School of Mines, Department of Geophysics, Golden, CO 80401, USA.

E-mail addresses: arevil@mines.edu (A. Revil), jeppehim@mymail.mines.edu (J.D. Eppehimer), mskold@mines.edu (M. Skold), marios.karaoulis@gmail.com (M. Karaoulis), lgodinez@mymail.mines.edu (L. Godinez), mprasad@mines.edu (M. Prasad).

0021-9797/$ - see front matter © 2013 Elsevier Inc. All rights reserved.
http://dx.doi.org/10.1016/j.jcis.2013.01.015

2. The diffuse layer "Standard" polarization model

2.1. Rationale

In this section, we provide the rationale of the standard model of Dukhin and Shilov [4–7] and its refinements. The standard model was developed to understand low-frequency dielectric dispersion (α-polarization) of colloids. It based on the following assumptions: (1) a Gouy–Chapman diffuse layer surrounds insulating grains (spheres, rods, or ellipsoids can be considered) and the densities of the counterions and co-ions follow Bolzmann statistics, and there are considered to be point charges, (2) the background electrolyte is a symmetric 1:1 electrolyte (e.g., NaCl), (3) the porous material is homogeneous and isotropic, (4) all the equations are linearized considering first-order perturbations only, (5) electroosmotic effects can be taken into accounts modifying the apparent mobility of the counterions and co-ions of the diffuse layer [15], and (5) no Stern layer is considered (see Section 3).

The set of local coupled equations to upscale with proper microscopic and macroscopic boundary conditions is (1) the Nernt-Planck equation, (2) the Stokes equation (inertial effects are neglected, so the flow is laminar) or alternatively the Navier–Stokes equation accounting for the inertial term, and (3) the local form of the Maxwell equations, which, for the problem of interest (<50 kHz), can be taken in the quasi-magnetostatic approximation. The electrical field is considered to be harmonic, and the field equations can be solved in the frequency domain or in the Laplace domain.

Modeling the low-frequency complex conductivity of granular media is a two-step process involving (1) the modeling of the dipole moment of a single grain (or type of grains) and (2) upscaling the solution for a water-saturated pack of grains or a colloidal suspension. The two operations are completely decoupled. Usually, in colloidal chemistry, researchers used a consistent approximation rather than the differential effective medium theory because they are dealing with dilute suspensions. The goal of the upscaling is to obtain an expression of the low-frequency complex conductivity σ^* (or alternatively the low-frequency dielectric constant) of the granular material defined as,

$$\sigma^* = |\sigma| \exp(i\varphi) = \sigma' + i\sigma''. \tag{1}$$

The term $|\sigma|$ denotes the amplitude of the electrical conductivity (in S m^{-1}), while φ describes the phase lag (usually reported in mrad) between the current and the electrical field. The terms σ' and σ'' denote the real (in-phase) and imaginary (quadrature) components of the conductivity (both expressed in S m^{-1}), and i denotes the pure imaginary number. The relationships between the in-phase and quadrature conductivities and the amplitude and phase are given by $|\sigma| = \sqrt{\sigma'^2 + \sigma''^2}$ and $\varphi = \mathrm{atan}(\sigma''/\sigma')$. Because the phase is small (smaller than 100 mrad in amplitude below 10 kHz), the phase is often approximated by $\varphi \approx \sigma''/\sigma'$.

There are many refinements of the standard model. For instance, Grosse [4] developed recently an extension of the standard model for non-symmetric electrolytes, and Aranda-Rascón et al. [16] developed the theory to account for the finite size of the ions. Carrique et al. [17] developed a cell approach for concentrated colloids accounting for particle–particle interactions. They, however, claim that a dynamic Stern layer would be required to improve the theory. Pride [15] looked at the effect of electroosmosis on the frequency-dependent complex conductivity. For simple supporting 1:1 electrolytes, it was concluded in [18] that electroosmosis can be taken into account by considering an apparent mobility $B_{(\pm)}$ for cations (+) and anions (−) defined by

$$B_{(\pm)} = \beta_{(\pm)} + \frac{2\varepsilon_f k_b T}{\eta_f e}. \tag{2}$$

in the specific surface conductivity associated with the electrical diffuse layer. In Eq. (2), $\varepsilon_f = (80 \times 8.854) \times 10^{-12}$ F m^{-1} denotes the dielectric constant of water, k_b denotes the Boltzmann constant (1.3807×10^{-23} J K^{-1}), T is the absolute temperature (in K), e denotes the elementary charge (1.6×10^{-19} C), η_f denotes the dynamic viscosity of the pore water (10^{-3} Pa s), and $\beta_{(\pm)}$ denotes the true mobility characterizing the electromigration of cations and anions in water (e.g., $\beta_{(+)}$ (Na^+, 25 °C) = 5.2×10^{-8} m^2 s^{-1} V^{-1}). The last term of Eq. (2) is on the order of 0.4×10^{-8} m^2 s^{-1} V^{-1}. This means that the apparent mobilities of the ions in the diffuse layer can be slightly higher than the true mobility of the same ions in water but the difference is very small, and electroosmosis is not expected to play a big role.

2.2. Limitations

It was realized in the nineties that this standard model was unable to explain most experimental data even for dilute colloidal suspensions [6,8]. The problems with the standard models are the following: (1) a complete analysis of the equations shows that the low-frequency response associated with the diffuse layer should be non-linear, but harmonic distortions are hardly observed at low frequencies for sandy and clayey materials, and (2) there are many systems (like clays) in which an important fraction (>85%) of the countercharge is located in the Stern layer and not in the diffuse layer.

Zukoski and Saville [19,20] and later Lyklema [9] introduced a dynamic Stern layer model that started to be used, in concert with the standard model, to describe low-frequency induced polarization of colloids [5,21]. In the next section, we will give the rationale for a Stern layer polarization model and provide a simple, semiempirical way to describe low-frequency polarization of porous media.

3. A simple Stern layer model

Our goal is to develop below a simple yet accurate model of the low-frequency complex conductivity of porous materials based on the polarization of the Stern layer. This model can be connected to the interfacial electrochemistry of the mineral surface (complexation models). We first focus on providing the rationale for a Stern layer-based polarization model (Section 3.1), then we describe the maximum amplitude of low-frequency polarization (Section 3.2), we couple the polarization model to a simple speciation model for clay minerals (Section 3.3), and finally, we provide a simple frequency-dependent polarization model (Section 3.4).

3.1. Rational for the Stern layer polarization model

In silica sands and clays, the double layer coating the grains is composed of not only a diffuse layer but also a Stern layer of sorbed counterions including inner-sphere and outer-sphere ligands. The existence of the Stern layer of weakly sorbed counterions is demonstrated by molecular dynamic simulations and corresponds to a condensation of the ions on the mineral surface breaking down the Boltzmann statistics [22,23].

We consider an external electrical field varying with time as $\mathbf{E} = \mathbf{E}_0 \exp(i\omega t)$. The conservation of ionic species along the mineral surface in the Stern layer is,

$$\frac{\partial \Gamma_{(+)}}{\partial t} = -\nabla_S \cdot \mathbf{j}_{(+)}, \tag{3}$$

where $\Gamma_{(+)}$ denotes the concentration of the weakly sorbed cations (in mol m^{-2}) at the mineral surface (density of counterions per surface area), ∇_S denotes a surface divergence with respect to the curvilinear coordinates describing the mineral surface, and $\mathbf{j}_{(+)}$ is the

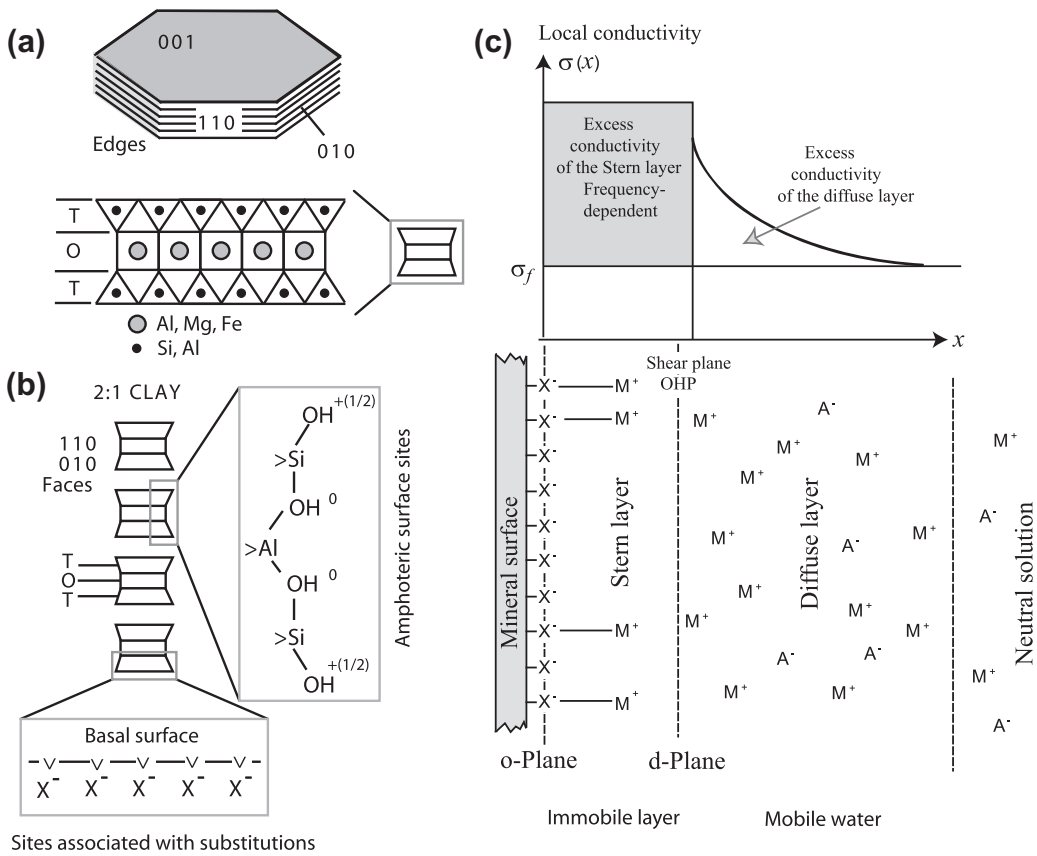

Fig. 1. Double layer associated with clay minerals. (a) TOT structure of clay minerals (T stands for the tetrahedral layer, O stands for the Octohedral layer). (b) The charge on the surface of the clay minerals depends on the amphoteric sites located on the edges of the clay crystals and negative sites associated with isomorphic substitutions in the crystalline framework of the clay minerals in the T- and O-layers. These isomorphic substitutions are responsible for the charge on the surface of the basal planes. c. The mineral charge is compensated by counterions (M^+) and coions (A^-) forming a double layer. This double layer comprises a layer of sorbed counterions (the Stern layer) and a diffuse layer.

flux density of the weakly sorbed cations along the mineral surface (in mol s^{-1} m^{-1}). The electrostatic equations obeyed by the electrical field in the low-frequency limit of the Maxwell equations are,

$$\nabla \cdot \mathbf{E} = \frac{\rho}{\varepsilon}, \tag{4}$$

$$\nabla \times \mathbf{E} = 0, \tag{5}$$

where ε denotes the dielectric constant in the Stern layer and ρ is the volumetric charge density. Eq. (5) implies in turn that the electrical field can be derived from an electrostatic potential ψ. As shown in [15] and [18], the electroosmotic velocity is zero on the surface of the grains, so it should not be accounted for in the flux densities on the mineral surface. The flux of cations along the mineral surface is therefore given by the classical Nernst–Planck local equation,

$$\mathbf{j}_{(+)} = -\frac{\beta^S_{(+)}\Gamma_{(+)}}{|q_{(+)}|}\nabla_S\tilde{\mu}_{(+)}, \tag{6}$$

$$\mathbf{j}_{(+)} = --\frac{\beta^S_{(+)}\Gamma_{(+)}}{|q_{(+)}|}\nabla_S(q_{(+)}\psi + k_bT\ln\Gamma_{(+)}), \tag{7}$$

$$\mathbf{j}_{(+)} = -\frac{\beta^S_{(+)}}{|q_{(+)}|}(q_{(+)}\Gamma_{(+)}\nabla_S\psi + k_bT\nabla_S\Gamma_{(+)}), \tag{8}$$

where $\tilde{\mu}_{(+)}$ denotes the electrochemical potential of the weakly sorbed cations, ∇_S denotes a surface gradient along the mineral surface, $\beta^S_{(+)}$ denotes the (Stern layer) ionic mobility of the weakly sorbed cations, and $q_{(+)} = (\pm 1)z_{(+)}e$ is their charge ($z_{(+)}$ is the unsigned valence). The tangential mobility of the weakly sorbed counterions is confirmed by nuclear magnetic resonance (NMR) spectroscopy (e.g., [24] in the case of sodium on silica).

According to Eq. (6), the lateral transport of the counterions in the Stern layer by electromigration is coupled to diffusion. In other words, the flux density is controlled by the gradient of the electrochemical potential $\tilde{\mu}_{(+)}$ of the weakly sorbed cations in the Stern layer, which comprises an electrostatic term and a concentration gradient term (an activity gradient term for non-ideal solution). Combining Eqs. (3) and (6) yields,

$$\frac{\partial\Gamma_{(+)}}{\partial t} = \frac{\beta^S_{(+)}}{|q_{(+)}|}\nabla_S\cdot\left(q_{(+)}\Gamma_{(+)}\nabla_S\psi + k_bT\nabla_S\Gamma_{(+)}\right). \tag{9}$$

Therefore, both the concentration gradient and the imposed electrical field are locally tangential to the mineral surface. Note that the electrical field resulting from the electrical double layer is normal to the mineral surface, and therefore, the two electrical fields are normal to each other. Concentration gradients and the electrical field provide the driving forces for the migration of the counterions along the Stern layer. The first boundary condition results from the continuity of the tangential component of the electrical field at the interface between the Stern layer and the diffuse layer. The second boundary condition results from the fact that the surface of the grain is insulating and therefore impervious to the transport of the counterions. For spherical grains, Gauss's law states [25],

$$\left(-\varepsilon\frac{\partial\psi}{\partial r}\right)_{r=d/2} = Q_0 + Q_\beta, \tag{10}$$

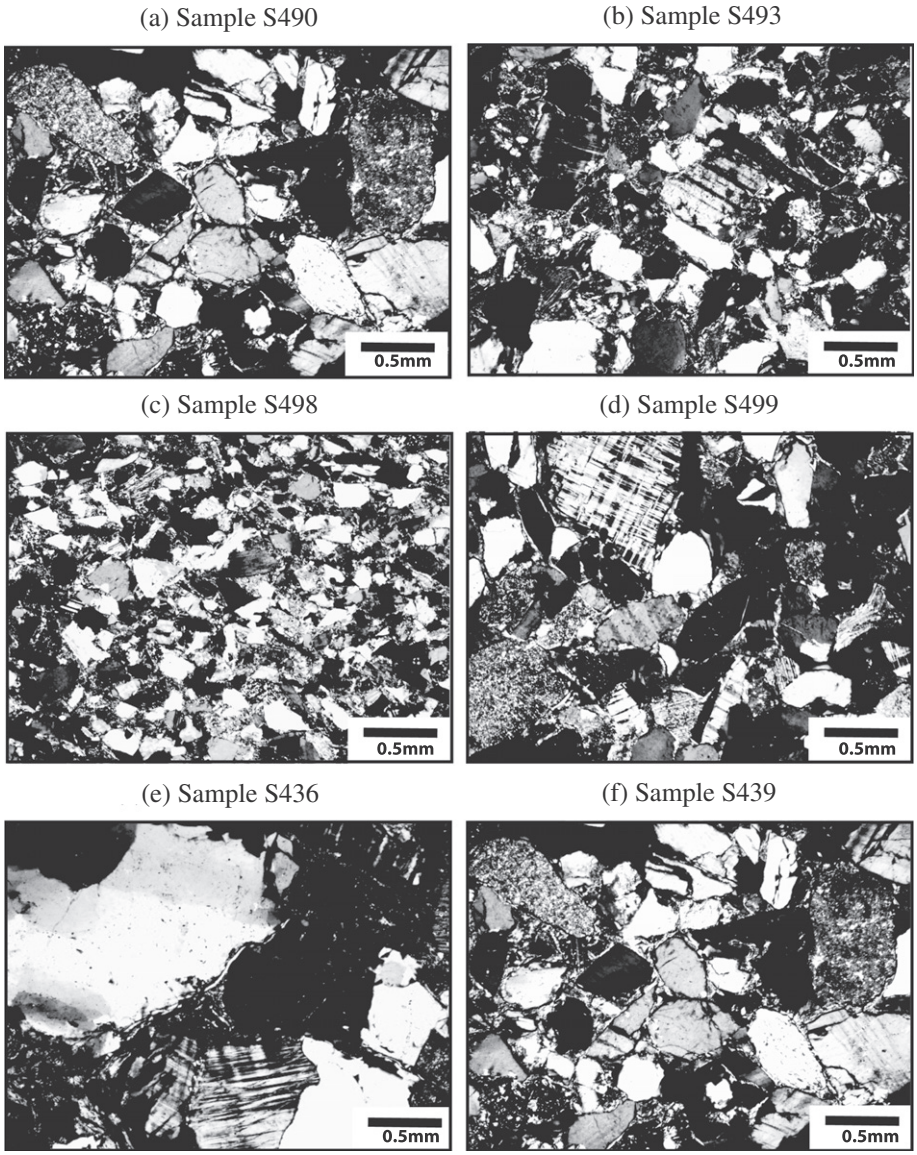

Fig. 2. Thin section photomicrographs of the six samples. (a) Medium to very coarse, poorly sorted, arkosic sandstone. (b) Very fine to medium, moderately sorted, subarkosic sandstone. (c) Very fine to medium, moderately to well-sorted, subarkosic sandstone. (d) Fine to very coarse, poorly sorted, arkosic sandstone. (e) Poorly sorted sandy conglomerate. (f) Clay with silt and very fine sand (mudstone).

where Q_0 is the mineral surface charge density (C m^{-3}), Q_β is the charge density of the Stern layer (C m^{-3}), and r is the radial distance from the center of the spherical grain of diameter d. These equations can be solved analytically [5] or numerically [25]. Rosen et al. [25] considered in their model the possible exchange of counterions between the Stern layer and the diffuse layer.

The Stern layer model would involve the following predictions: (1) a strong control of the polarization response by the cation exchange capacity or alternatively the specific surface area of the material, (2) a reduced mobility for the electromigration of the counterions at the surface of clay minerals, and (3) a reduced diffusivity for the relaxation time (rather than the mutual diffusion coefficient used in the standard model). We will discuss in the next section, a model to capture the magnitude of the Stern layer polarization of the clay minerals.

3.2. Expression for the complex conductivity

According to the Stern layer polarization model developed by Revil and co-workers [5,13,14,26], the complex conductivity of a granular material can be written as,

$$\sigma^* = \frac{1}{F}\sigma_w + \sigma_S^*. \tag{11}$$

$$\sigma^* = \sigma_w\left(\frac{1}{F} + \mathrm{Du}^*\right). \tag{12}$$

where F denotes the formation factor (dimensionless), σ_w denotes the (real) electrical conductivity of the pore water (in S m^{-1}), σ_S^* denotes the complex-valued surface conductivity (in S m^{-1}), and $\mathrm{Du}^* \equiv \sigma_S^*/\sigma_w$ denotes the complex-valued Dukhin number (unitless). The electrical formation factor F is related to the connected porosity ϕ by Archie's law $F=\phi^{-m}$, and m denotes the cementation exponent [27]. A physical explanation of the formation factor in terms of pore space topology is given in Appendix A.

As mentioned above, the electrical double layer comprises the Stern layer of weakly sorbed counterions (outer-sphere complexes) and the diffuse layer (see Fig. 1). According to the Stern layer polarization model, the complex surface conductivity and the complex Dukhin number are given by [12],

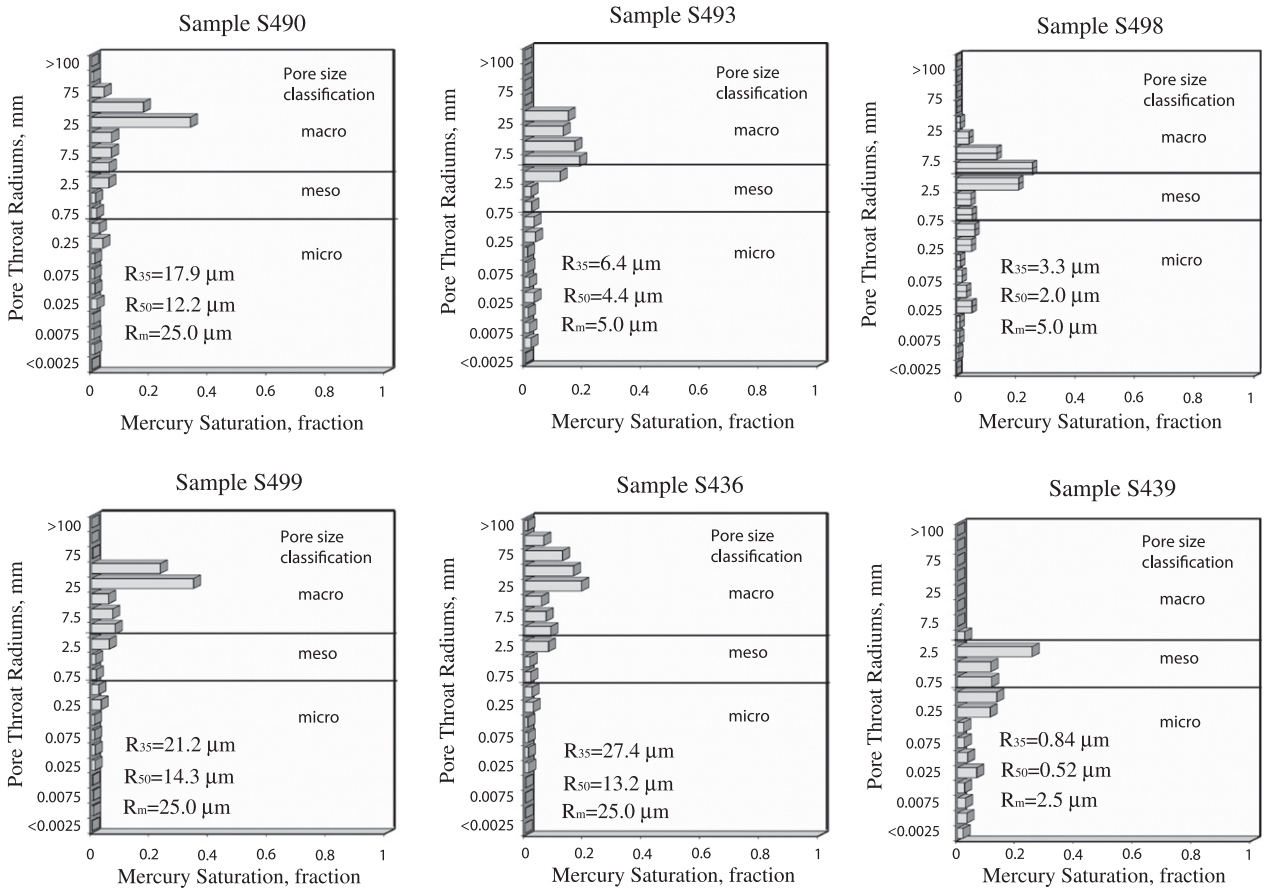

Fig. 3. Pore size distribution from mercury intrusion experiments. We have also indicated the median values of the pore size distributions R_{50} and the modal pore throat size R_m. The mudstone corresponds to the core sample with the smallest pore sizes.

Table 1
Description of the core samples in terms of petrology, porosity, permeability, and grain mass density. When the grain density is not directly measured, it is assumed equal to the grain density of silica (2650 kg m^{-3}).

Sample	Type	Porosity (–)	Permeability (mD)	Density grains (kg m^{-3})
S499	Coarse sandstone	0.265	1103	2596
S498	Medium sandstone	0.206	35.9	2635
S490	Coarse sandstone	0.233	635	2602
S493	Medium silty sandstone	0.232	115	2619
S439	Mudstone	0.208	2.62	2613
S436	Coarse sandstone	0.306	1623	2619
S9	Saprolite	0.48	16	–
S16	Saprolite	0.49	5.0	–
S22	Saprolite	0.43	7.7	–
S14	Saprolite	0.39	54.1	–
S20	Saprolite	0.33	10.2	–
S18	Saprolite	0.36	54.0	–
S5	Saprolite	0.45	21.4	–
S10	Saprolite	–	–	–
S12	Saprolite	0.37	29.7	–
S7	Saprolite	0.48	326	–

$$\sigma_S^* = \frac{2}{3}\rho_g \mathrm{CEC}\left[B_{(+)}(1-f) - i\beta_{(+)}^S f\right], \tag{13}$$

$$\mathrm{Du}^* = \frac{2}{3}\left(\frac{\rho_g \mathrm{CEC}}{\sigma_w}\right)\left[B_{(+)}(1-f) - i\beta_{(+)}^S f\right]. \tag{14}$$

where f denotes the fraction of counterions in the Stern layer (dimensionless), ρ_g denotes the grain density (typically 2650 kg m^{-3}), $B_{(+)} \approx \beta_{(+)}$ denotes the apparent mobility of the counterions in the diffuse layer (see Section 2), and $\beta_{(+)}^S$ denotes the mobility of the counterions in the Stern layer. For clay minerals, Revil [12] found recently $\beta_{(+)}^S$ (25 °C, Na^+) = 1.5×10^{-10} m^2 s^{-1} V^{-1} while for silica $\beta_{(+)}^S$ (Na^+, 25 °C) $\approx 5.2 \times 10^{-8}$ m^2 s^{-1} V^{-1} (these values will be discussed further below in Section 5.2). The salinity dependence of the partition coefficient f is discussed in Section 3.3 below.

The surface conductivity and the Dukhin (dimensionless) number are defined as the real part of the complex surface conductivity and the real part of the complex Dukhin number,

$$\sigma_S = \mathrm{Re}[\sigma_S^*], \tag{15}$$

Table 2
Petrophysical Properties of the core samples. S_{Sp} (in m^2/g) denotes the specific surface area determined by the BET method, F (–) denotes the intrinsic formation factor determined from the conductivity measurements performed at different pore water salinities, and σ'_S (in S m^{-1}) denotes the surface conductivity from the same data.

Sample	Specific surface area (m^2 kg^{-1})	CEC (cmol kg^{-1})	Formation factor (–)	Surface conductivity (10^{-4} S m^{-1})	Quadrature conductivity (S m^{-1})[a]
S499	48.6	–	5.6 ± 0.4	3.3 ± 0.7	-4×10^{-3}
S498	5020	–	9.0 ± 0.8	390 ± 90	-1.6×10^{-3}
S490	10,100	–	12.1 ± 0.4	400 ± 130	-1.5×10^{-3}
S493	10,100	–	18.3 ± 0.4	570 ± 90	-2.5×10^{-3}
S439	15,200	–	13.3 ± 0.7	290 ± 90	-1.5×10^{-3}
S436	88	–	4.0 ± 0.3	–	-2×10^{-3}
S9	14,957	–	4.1 ± 0.3	39 ± 6	-1.1×10^{-3}
S16	9261	–	5.9 ± 0.1	95 ± 2	-1.7×10^{-3}
S22	18,174	–	4.4 ± 0.5	376 ± 34	-1.6×10^{-3}
S14	14,834	5.24 ± 0.86	7.1 ± 2.5	386 ± 157	-1.2×10^{-3}
S20	9.329	5.19 ± 0.84	5.1 ± 0.2	237 ± 23	-1.2×10^{-3}
S18	13,659	7.86 ± 0.42	7.3 ± 2.6	633 ± 169	-1.6×10^{-3}
S5	24,321	8.57 ± 0.18	4.4 ± 0.3	39 ± 32	-1.0×10^{-3}
S10	29,091	7.95 ± 0.08	4.1 ± 0.8	–	-1.7×10^{-3}
S12	18,353	6.85 ± 0.01	5.1 ± 0.2	148 ± 15	-1.3×10^{-3}
S7	17,102	4.96 ± 0.87	3.7 ± 0.3	14 ± 13	-4.0×10^{-4}

[a] 1 Hz or at the peak frequency. Pore water conductivity (NaCl): about 0.1 S m^{-1}.

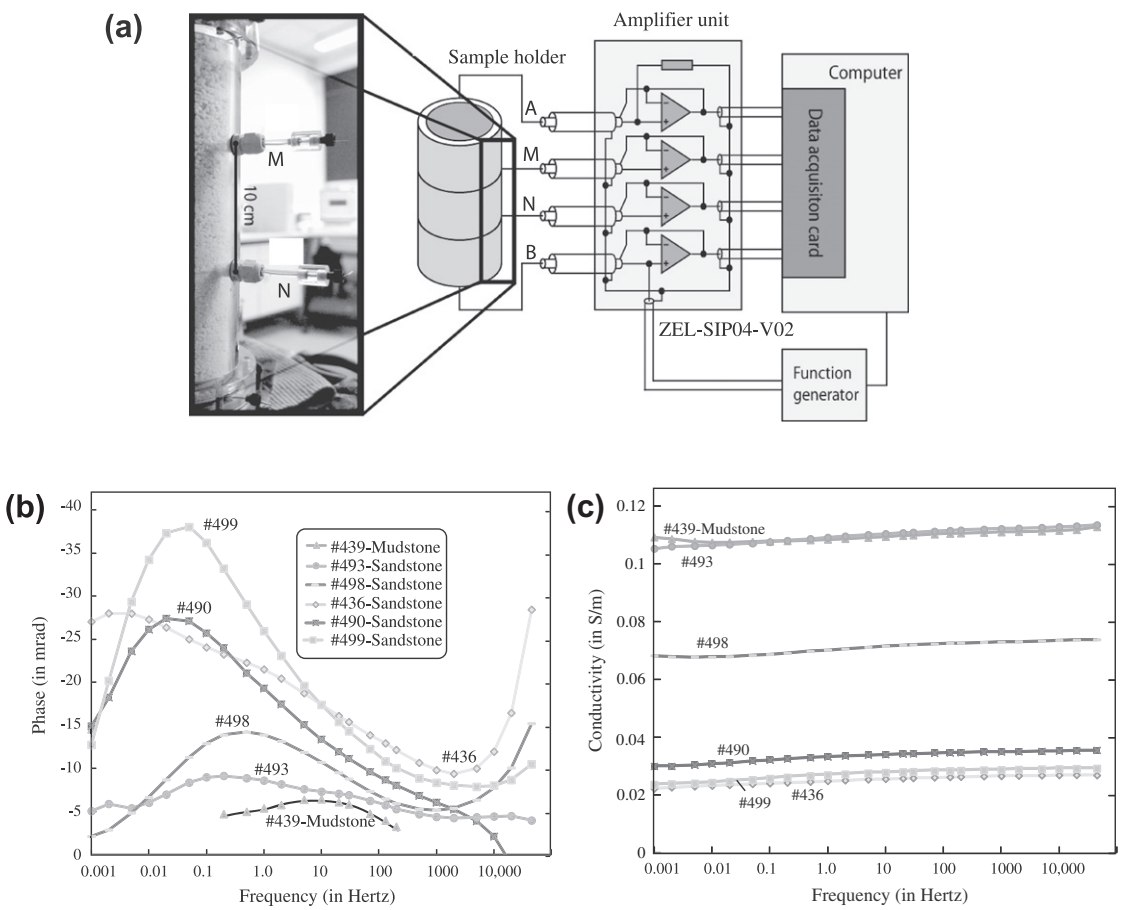

Fig. 4. Raw in situ pore water conductivity data. (a) Sketch of the high-sensitivity impedance meter used to collect the SIP measurements (ZEL-SIP04-V02). Adapted from [34,35]. The measurements were collected using a Wenner-type array: A and B correspond to the current electrodes while M and N correspond to the potential electrodes. (b) Measured phase versus frequency for the six samples saturated with native groundwater (for typical site groundwater quality see Table 2). (c) Electrical conductivity versus frequency for the six samples saturated with the native groundwater (see Table 2, conductivity at room temperature: 0.048 ± 0.013 S m^{-1}).

$$\mathrm{Du} = \mathrm{Re}[\mathrm{Du}^*], \tag{16}$$

respectively.

The in-phase conductivity normalized by the pore water conductivity, and the phase obey therefore the following relationships,

$$\frac{\sigma'}{\sigma_w} = \frac{1}{F} + \mathrm{Du}, \tag{17}$$

$$\varphi \approx -\frac{\frac{2}{3}F\beta^S_{(+)}f\rho_g\mathrm{CEC}}{\sigma_w + \frac{2}{3}B_{(+)}F(1-f)\rho_g\mathrm{CEC}}, \tag{18}$$

respectively. Following [12,14], Eq. (18) for the phase lag can be also approximated by,

$$\varphi \approx -\frac{\beta^S_{(+)}fQ_V}{\sigma_w + B_{(+)}(1-f)Q_V}, \tag{19}$$

Table 3
Typical composition of the natural groundwater (GW) for the sandstones and saprolites used to perform some of measurements. TDS: total dissolved solids.

Parameter	Units	Sandstone	Saprolite
TDS	mg L^{-1}	318	433
Conductivity	μS cm^{-1}	479	64
pH	–	8.1	7.5
Alkalinity	mg L^{-1}	109	175
Na^+	mg L^{-1}	30.6	2.7
K^+	mg L^{-1}	3.9	2.0
Ca^{2+}	mg L^{-1}	65.0	26
Mg^{2+}	mg L^{-1}	3.1	5.0
Cl^-	mg L^{-1}	6.0	3.5
HCO_3^-	mg L^{-1}	123	220
SO_4^{2-}	mg L^{-1}	132	90

To go from Eq. (18) to Eq. (19), we use the following relationship $F \approx (3/2)(1-\phi)/\phi$ (see [10]). The total charge per unit volume (total excess charge density) is related to the cation exchange capacity (charge per unit mass of grains) of the material by,

$$Q_V \equiv \rho_g \left(\frac{1-\phi}{\phi}\right) \mathrm{CEC}. \tag{20}$$

In the next section, we describe how the partition coefficient depends on the salinity.

3.3. Influence of surface chemistry

We propose here a simple model to describe the salinity dependence of the partition coefficient *f*. We consider the sorption of sodium in the Stern layer of clays and the dissociation of protons,

$$> SH^0 \Longleftrightarrow\ > S^- + H^+, \tag{21}$$

$$> S^- + Na^+ \Longleftrightarrow\ > S^-Na^+, \tag{22}$$

where >S refers the surface (amphoteric) sites attached to the crystalline framework, H^0 are (immobile) protons, while the weakly sorbed Na^+ are considered to be mobile in the Stern layer. The equilibrium constants for the reactions (21) and (22) are given by,

$$K_{Na} = \frac{\Gamma^0_{SNa}}{\Gamma^0_{S^-}[Na^+]^0}, \tag{23}$$

$$K_H = \frac{\Gamma^0_{S^-}[H^+]^0}{\Gamma^0_{SH}}. \tag{24}$$

The conservation equation for the surface species is given by,

$$\Gamma^0_S = \Gamma^0_{SNa} + \Gamma^0_{SH} + \Gamma^0_{S^-} + \Gamma^0_X, \tag{25}$$

where Γ^0_S denotes the total surface site density (including the charge associated with isomorphic substitutions in the crystalline framework), Γ^0_{SNa}, $\Gamma^0_{S^-}$, and Γ^0_{SH} represent the surface charge density of the sites $>S^-Na^+$, $>S^-$, and $>SH^0$ respectively, and Γ^0_X represents the number of equivalent sites corresponding to isomorphic substitutions (all expressed in sites m^{-2}). To simplify the notations, we write $pH = -\log_{10}[H^+]$, while $[Na^+] = C_f$ denotes the salinity of the pore water solution. The resolution of the previous set of equations, Eqs. (23)–(25), is straightforward and yields,

$$\Gamma^0_{SH} = \frac{\Gamma^0_S - \Gamma^0_X}{1 + \frac{K_H}{10^{-pH}}(1 + C_f K_{Na})}, \tag{26}$$

$$\Gamma^0_{S^-} = \frac{(\Gamma^0_S - \Gamma^0_X)K_H/10^{-pH}}{1 + \frac{K_H}{10^{-pH}}(1 + C_f K_{Na})}, \tag{27}$$

$$\Gamma^0_{SNa} = \frac{(\Gamma^0_S - \Gamma^0_X)C_f K_{Na} K_H/10^{-pH}}{1 + \frac{K_H}{10^{-pH}}(1 + C_f K_{Na})}. \tag{28}$$

All the charged sites that are not compensated in the Stern layer needs to be compensated in the diffuse layer. Therefore, the fraction of the counterions in the Stern layer is defined by the following equation,

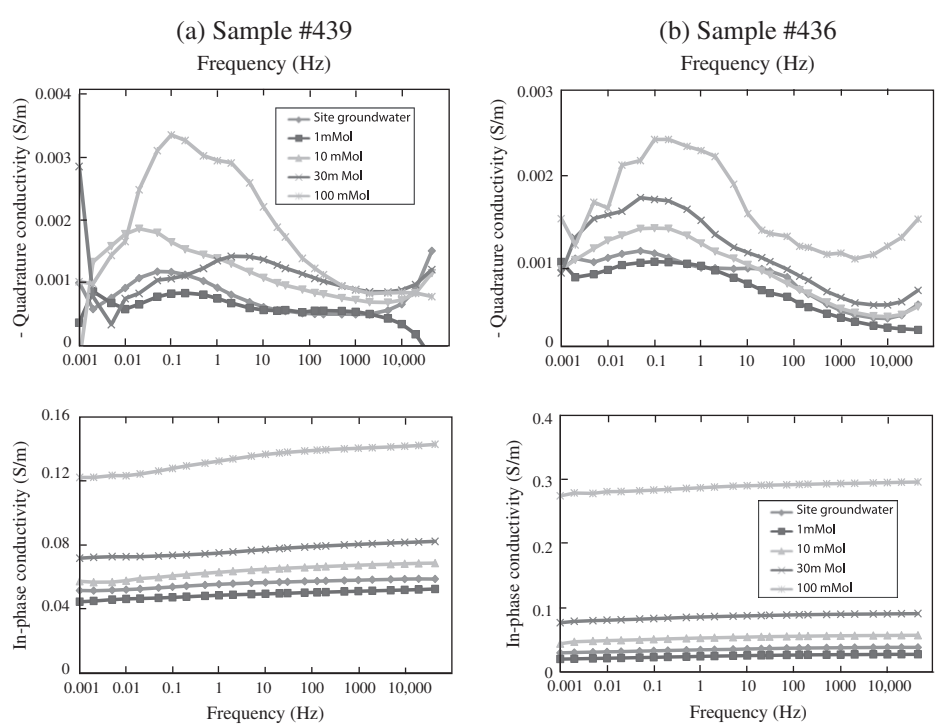

Fig. 5. Example of spectra for samples S439 (mudstone) and S436 (sandy conglomerate). These data show a well-defined peak frequency in the quadrature conductivity.

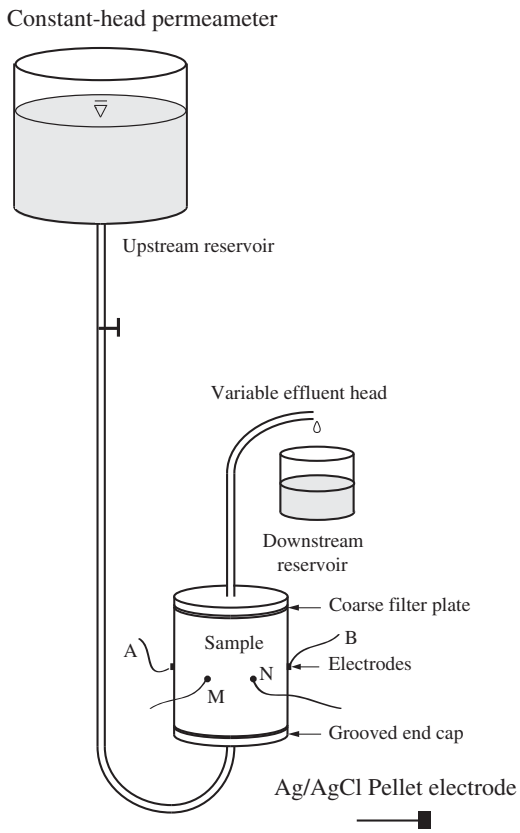

Fig. 6. Sketch of the equipment used for the permeability and electrical measurements. Constant head permeameter. The non-polarizing Ag/AgCl electrodes for the measurement of the complex conductivity are organized in a Wenner array (A and B are the current electrodes, M and N are the potential electrodes). The electrodes ABMN are located in the middle of the sample holder (see comparison with the sample holder shown in Fig. 4). We use the same impedance meter as shown in Fig. 4 (ZEL-SIP04-V02).

$$f = \frac{\Gamma^0_{\mathrm{SNa}}}{\Gamma^0_{\mathrm{SNa}} + \Gamma^0_{\mathrm{S^-}} + \Gamma^0_{\mathrm{X}}}. \tag{29}$$

$$f = f_M \left\{ \frac{C_f K_{\mathrm{Na}}}{f_M(1 + C_f K_{\mathrm{Na}}) + (1 - f_M)\left[1 + C_f K_{\mathrm{Na}} + \frac{10^{-\mathrm{pH}}}{K_H}\right]} \right\}, \tag{30}$$

where f_M denotes the highest value of f reached at high salinities,

$$f_M = \lim_{C_f >> 1/K_{\mathrm{Na}}} f = 1 - \frac{\Gamma^0_{\mathrm{X}}}{\Gamma^0_{\mathrm{S}}}. \tag{31}$$

The value of f_M is about 0.99 for kaolinite, 0.90 for illite, and 0.85 for smectite (see [12]). At high pH values (typically near-neutral pH or higher),

$$f \approx f_M \left(\frac{C_f K_{\mathrm{Na}}}{1 + C_f K_{\mathrm{Na}}} \right). \tag{32}$$

We look now for the pH dependence of the CEC. The CEC is defined by,

$$\mathrm{CEC} = \frac{e}{f_M} \left(\Gamma^0_{\mathrm{SNa}} + \Gamma^0_{\mathrm{S^-}} + \Gamma^0_{\mathrm{X}} \right) S_{sp}. \tag{33}$$

where S_{sp} correspond to the specific surface area (in $\mathrm{m^2\,kg^{-1}}$) and e the elementary charge. After some algebraic manipulations and simplification, we obtain,

$$\mathrm{CEC}(\mathrm{pH}, \mathrm{C_f}) = \left(\frac{K_H + C_f K_{\mathrm{Na}} K_H}{K_H + C_f K_{\mathrm{Na}} K_H + 10^{-\mathrm{pH}}} \right) \mathrm{CEC}_M. \tag{34}$$

$$\mathrm{CEC}_M = e \Gamma^0_{\mathrm{S}} S_{sp}. \tag{35}$$

where CEC_M corresponds to the maximum CEC at value at high pH values.

From Eqs. (1), (11), and (13), the quadrature conductivity is given by,

$$\sigma'' = -\frac{2}{3} \rho_g \beta^S_{(+)} f \mathrm{CEC}, \tag{36}$$

where the product of f by the CEC is given by $f\mathrm{CEC} = e\Gamma^0_{\mathrm{SNa}} S_{sp}$ (the quadrature conductivity is controlled by the density of weakly sorbed sodium counterions in the Stern layer). Starting with Eqs. (30), (34), (35), and (36), we obtain,

$$\sigma'' = \sigma''_M \left(\frac{C_f K_{\mathrm{Na}} K_{\mathrm{H}}}{10^{-\mathrm{pH}} + K_{\mathrm{H}}(1 + C_f K_{\mathrm{Na}})} \right), \tag{37}$$

$$\sigma''_M = -\frac{2}{3} \left(\rho_g \beta^S_{(+)} f_M e \Gamma^0_S \right) S_{sp}. \tag{38}$$

where σ''_M denotes the quadrature conductivity reached at high salinity and high pH. At high pH values, Eq. (37) can be approximated by

$$\sigma''_M \approx \sigma''_M \left(\frac{C_f K_{Na}}{1 + C_f K_{Na}} \right). \tag{39}$$

Eq. (39) offers a simple expression to compute the salinity dependence of the quadrature conductivity.

3.4. Influence of frequency

In the previous model, we have not accounted for the frequency dependence of the complex conductivity. Low-frequency induced polarization is classically described in terms of a Cole–Cole distribution given by (e.g., [10,28]),

$$\sigma^* = \sigma_\infty \left[1 - \frac{M}{1 + (i\omega\tau_{CC})^c} \right], \tag{40}$$

$$M = \frac{\sigma_\infty - \sigma_0}{\sigma_\infty}, \tag{41}$$

where M ($0 < M < 1$) denotes chargeability (dimensionless but usually expressed in $\mathrm{mV\,V^{-1}}$ when the measurements are obtained in the time-domain, σ_0 denotes the DC (Direct Current) electrical conductivity ($\omega = 0$), σ_∞ the high-frequency electrical conductivity ($\omega \gg 1/\tau_{CC}$), τ_{CC} denotes the Cole–Cole time constant, c denotes the Cole–Cole exponent for the complex conductivity. Expressions for σ_0 and σ_∞ that are compatible with the ones described above in Section 3.1 are provided in Appendix B. The case $c = 1/2$ corresponds to the Warburg impedance model, which corresponds in turn to have the Stern layer behaving as a leaking capacitance because of the sorption/desorption of counterions.

The in-phase and quadrature components of Eq. (40) are given by,

$$\sigma' = \sigma_\infty - \frac{1}{2} M_n \{ 1 - \frac{\sinh[c \ln(\omega\tau)]}{\cosh[c \ln(\omega\tau)] + \cos[\frac{\pi}{2}(1 - c)]} \}, \tag{42}$$

$$\sigma'' = -\frac{1}{2} \left\{ \frac{M_n \cos\left[\frac{\pi}{2}(1 - c)\right]}{\cos h[c \ln(\omega\tau)] + \sin\left[\frac{\pi}{2}(1 - c)\right]} \right\}. \tag{43}$$

where $M_n = M\sigma_\infty = \sigma_\infty - \sigma_0$ denotes the normalized chargeability of the material. Eqs. (42) and (43) can be used to invert complex conductivity spectra in terms of the four Cole–Cole parameters: $\rho_0 = 1/\sigma_0$, M, c, and τ_{CC}. The normalized chargeability is actually equal to the quadrature conductivity given by Eq. (39) at the peak frequency.

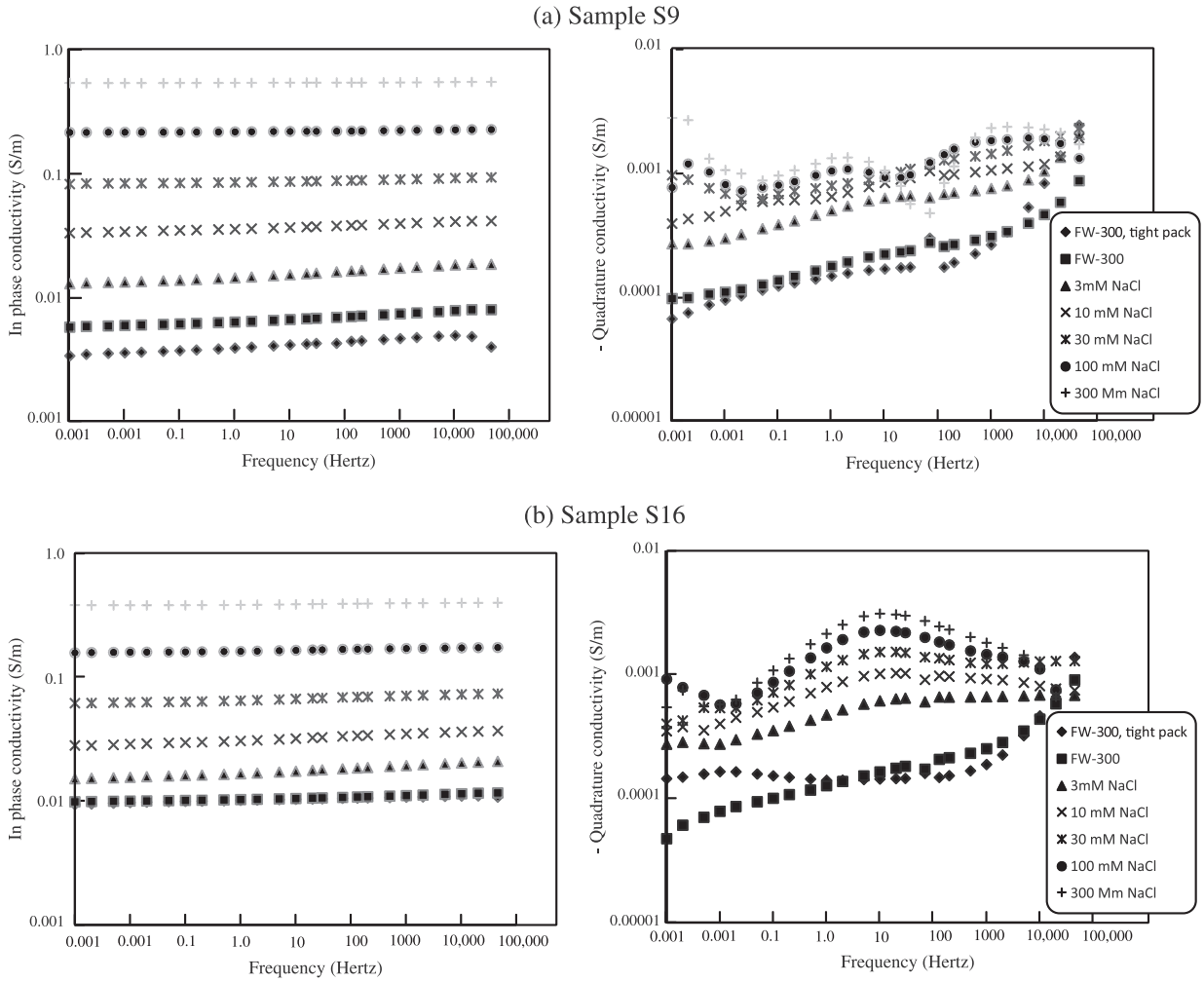

Fig. 7. In-phase and quadrature conductivities at different pore water salinities. pH values in the range 5–6. For sample S16, we observe that the quadrature conductivity peaks at the same frequency whatever the salinity of the NaCl solution.

The angular frequency of the phase peak is given by

$$\omega_{\text{peak}} = \left(\frac{\sigma_\infty}{\sigma_0}\right)^{1/2c} \frac{1}{\tau_{CC}} = \left(\frac{1}{1-M}\right)^{1/2c} \frac{1}{\tau_{CC}}. \tag{44}$$

If $M \ll 1$, then $\omega_{\text{peak}} \approx 1/\tau_{CC}$.

For clean sands, The Cole–Cole relaxation time was found to be controlled by the mean pore size of the material Λ according to [13]

$$\tau_{CC} = \frac{\Lambda^2}{2D^S_{(+)}}, \tag{45}$$

where $D^S_{(+)}$ denotes the diffusion coefficient of the counterions in the Stern layer (see Section 5.2).

4. Experimental data

In order to test further the Stern polarization model on natural porous media, we developed a new database of well characterized sandstones and saprolites. This database comprises 17 samples divided into two sets of materials: 11 unconsolidated saprolitic core samples and 6 weakly consolidated sandstones (including a mudstone).

4.1. Core samples

Six samples were collected from the Great Divide Basin (Wyoming). Five samples are grain supported sandstones with angular to subrounded grains (Fig. 2). Sample S439 is a mudstone (Fig. 2f). The pore size distributions of these materials were determined form mercury intrusion (Fig. 3).

Eleven saprolite samples were taken from the Oak Ridge National Laboratory (Tennessee). The saprolite results from the weathering of Middle Cambrian interbedded shale, siltstone, and limestone forming the parent rock material [29]. The sand and silt fractions (in weight) are grossly 50% and 30%, respectively, and the clay fraction is about 20% [30–33]. The clay is mainly illite with some mixed-layer illite–smectite clay minerals. The petrophysical properties of all the samples are reported in Tables 1 and 2.

4.2. Measurement of the complex conductivity

Complex conductivity measurements were performed using four electrodes. The complex impedance Z^* (in ohm) is defined as

$$Z^*(\omega) = \frac{U}{I} = |Z^*(\omega)|e^{i\varphi(\omega)}, \tag{46}$$

where U is the measured voltage difference between two electrodes M and N, I denotes the magnitude of the current injected/retrieved

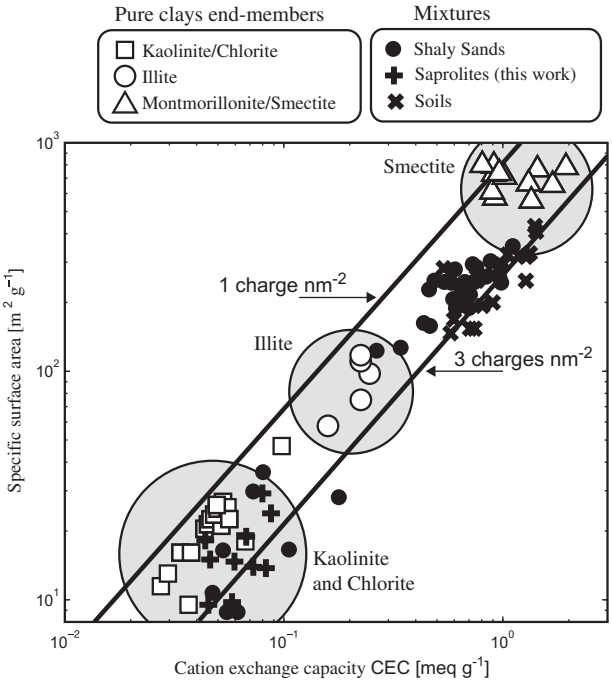

Fig. 8. Specific surface area versus CEC (in meq g^{-1} with 1 meq g^{-1} = 96,320 C kg^{-1} in SI units) for 18 saprolite core samples from the Oak Ridge background site. The two lines corresponds to 1–3 elementary charges per unit surface area. Data for the clay end-members are from: [41] to [48]. The soil data are from [49].

at electrodes A and B, and $|Z^*(\omega)|$ and $\varphi(\omega)$ denote the amplitude and the phase of the complex impedance, respectively. The complex resistivity $\rho^* = 1/\sigma^*$ (in Ω m) is related to Z^* by a geometrical factor K (in m): $\rho^*(\omega) = KZ^*(\omega)$. This geometrical factor K takes into account the position and dimensions of the electrodes and the insulating boundary conditions on the sample holder.

The electrical measurements were taken using a ZEL-SIP04-V02 impedance meter (Fig. 4a, see [34] for details on this apparatus and [35] for benchmark tests). Spectral induced polarization spectra were recorded at 25 frequencies from 1 mHz to 45 kHz, with repeatability checked by running samples twice, or running a limited frequency range several times. The accuracy of the instrument is ~0.1–0.3 mrad at frequencies below 1 kHz.

For the five sandstones and the mudstone, the following fluids were used to saturate the samples: (1) natural site groundwater (conductivity at 25 °C, 0.048 ± 0.013 S m^{-1}) and (2) the following NaCl solutions at 1 mM (measured conductivity 0.033 S m^{-1}), 10 mM (0.204 S m^{-1}), 30 mM (0.328 S m^{-1}), and 100 mM (1.125 S m^{-1}).

Ag–AgCl electrodes were used for both injection and potential electrodes. Most electrode arrays were circumferential with some being axially arranged. The spectra for the sandstone/mudstone samples saturated with the ground water (see composition in Table 3) are shown in Fig. 4b and c. The spectra obtained for Samples S439 and S436, at different salinities, are shown in Fig. 5. Saturation of the samples was done with a vacuum chamber.

For the saprolite core samples, we used the permeameter shown in Fig. 6. The reported pore water conductivity is the conductivity of the effluent once equilibrium has been reached at a given salinity with a NaCl solution. The complex conductivity of samples S14, S20, S18, S5, S10, S12, and S7 were measured with salinities at 10 mM, 30 mM, and 100 mM (NaCl), while the Samples S9, S16, and S22 were measured at the following salinities natural ground water (see Table 2, typical conductivity of the effluent comprised between 0.0064 and 0.0072 S m^{-1}), 3 mM (typical conductivity of the effluent 0.0390 S m^{-1}), 10 mM (typical conductivity of the effluent 0.12 S m^{-1}), 30 mM (typical conductivity of the effluent 0.32 S m^{-1}), 100 mM (typical conductivity of the effluent 0.90 S m^{-1}), and 300 mM (typical conductivity of the effluent 2.54 S m^{-1}) (NaCl solutions) plus using the ground water described in Table 2. We use the same impedance meter (ZEL-SIP04-V02), and we investigated the same frequency range than above for the sandstones and the mudstone. Some of the spectra are displayed in Fig. 7.

4.3. Determination of the permeability

For the sandstones and the mudstone, the permeability was determined from the mercury intrusion experiments using the Swanson approach [36]. The validity of this approach was checked on two samples for which the permeability was measured by a flow-through experiment. For instance for Sample S498, we obtain a Klinkenberg-corrected air permeability of 78 mD versus an estimated permeability of 87 mD using the Swanson approach. For Sample S493, we obtain a Klinkenberg-corrected air permeability of 25 mD versus an estimated permeability of 27 mD using the Swanson approach.

For the saprolite core samples, the permeability was directly estimated using the permeameter shown in Fig. 7 using flow-through experiments with the pore water. The permeability was measured at each salinity, and we found no dependence of the permeability on the salinity (potential swelling/shrinking effects associated with the presence of smectites could have been expected). All the data are reported in Table 1.

4.4. Measurement of the CEC and specific surface area

In addition to the complex conductivity measurements, we also performed cation exchange capacity (CEC) and specific surface area (using the BET method) measurements. The CEC measurements were performed on 7 saprolite core samples using a barium chloride solution to displace the cations sorbed to the clays (see protocol in [37]). All the seven samples were analyzed in duplicates with relative standard deviation less than 17%. The average measured CEC value of the samples ranges from 5.0 to 8.6 cmol kg^{-1} or $CEC_M = (4.8–8.3) \times 10^3$ C kg^{-1} (see measurements in Table 2).

Specific surface area measurements were performed with the BET method using nitrogen as the adsorbent gas. Measurements were collected using a surface area analyzer (Micromeritics ASAP 2020). The surface area of pores of the core samples was calculated using the Brunauer, Emmett, and Teller (BET)-theory [38,39]. The specific surface area measurements are reported in Table 2 for all the core samples.

In Fig. 8, we plot the specific surface area measurements of the seven saprolite core samples versus their cation exchange capacity. The ratio of the CEC by the specific surface area defines the equivalent charge per unit surface area: $Q_S = CEC_M/S_{sp}$ which is approximately equal to 0.32 C m^{-2} (two elementary charges per nm^2, [40]). In Fig. 8, our measurements are shown to be consistent with a broad range of literature data indicating a surface charge density comprised between 1 and 3 elementary charges per nm^2 for clay minerals [41–49].

5. Theory versus experimental data

In this section, we compare the model discussed in Section 3 with the experimental data described in Section 4. The following aspects of the model are tested: dependence of the complex conductivity on the salinity, specific surface area, cation exchange capacity, and pore size.

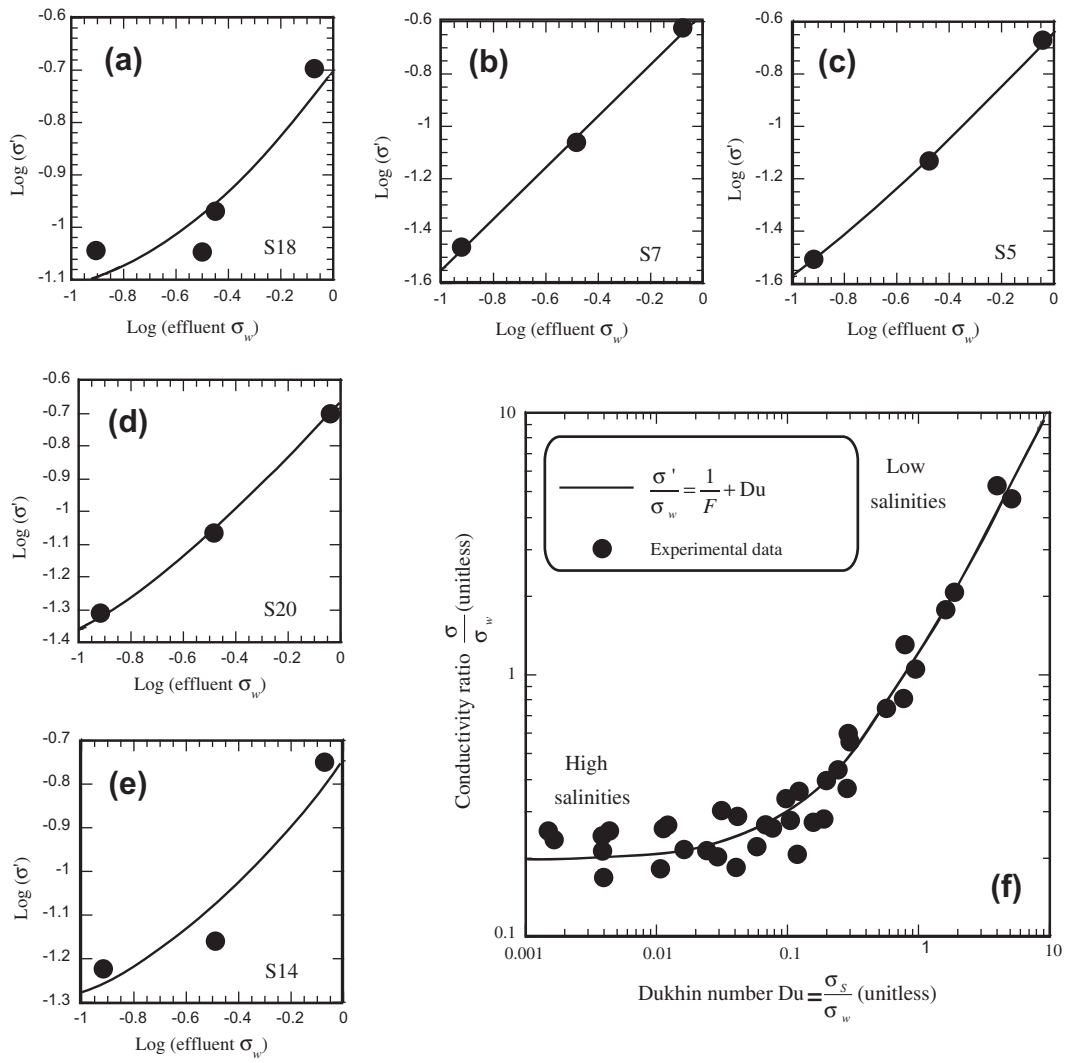

Fig. 9. Normalized conductivity versus the Dukhin number for all the saprolite core samples (pH ~ 5–6,) having the same range of formation factors 5.1 ± 1.0 (see Table 2). The measurements are reported at 1 Hz.

5.1. Dependence on the Dukhin number

From Eqs. (12) and (16), the in-phase conductivity can be written as,

$$\sigma' = \sigma_w\left(\frac{1}{F} + \mathrm{Du}\right). \tag{47}$$

Therefore, the normalized conductivity (σ'/σ_w) depends only on the unitless Dukhin number Du and the formation factor F. In Fig. 9, we plot the normalized conductivity versus the Dukhin number for three saprolite core samples having the same formation factor. All the data fall along the trend predicted by Eq. (47) showing that a linear conductivity model provides a correct representation of the electrical conductivity at different pore water conductivities.

5.2. Dependence on the specific surface area

According to Eq. (38), the plateau of the quadrature conductivity is also a measure of the specific surface area (in kg m^{-2}) of the porous material. From Eq. (38), we have,

$$\sigma'' = -aS_{Sp}, \tag{48}$$

$$a = \frac{2}{3}\beta^{S}_{(+)} f \rho_g Q_S. \tag{49}$$

where Q_S denotes the charge density of the mineral surface (0.32 C m^{-2}, see Section 4.4) and ρ_g denotes the mass density of the grains (solid phase). The mobility of the counterions in the Stern layer is vastly different for silica and aluminosilicates, that is, clay minerals [12,13], and such different property materials should therefore yield two distinct master curves with very different values of the coefficient a.

For clayey sands, taking $\beta^{S}_{(+)}$ (Na$^+$) = 1.5 × 10^{-10} m^2 s^{-1} V^{-1} at 25 °C, f = 0.90, Q_S = 0.32 C m^{-2}, ρ_g = 2650 kg m^{-3}, we can write $\sigma'' \approx -aS_{Sp}$ with a = 7.6 × 10^{-8} S kg m^{-3} [12]. For the clean sands and sandstones, if we use $\beta_{(+)}$ (Na$^+$) = 5.2 × 10^{-8} m^2 s^{-1} V^{-1}, f = 0.50, Q_S = 0.64 C m^{-2}, ρ_g = 2650 kg m^{-3}, we obtain a = 2.9 × 10^{-5} S kg m^{-3} [13]. For the clean sands and sandstones, the specific surface areas were calculated from the median grain diameters, (d_{50}) using $S_{Sp} = 6/(\rho_g d_{50})$ where ρ_g = 2650 kg m^{-3} denotes the density of the silica grains.

In Fig. 10, we plot the quadrature conductivity versus the specific surface area of the core samples investigated in the present study together with additional data from the literature. The datasets split into two distinct linear trends: one for clean sands and

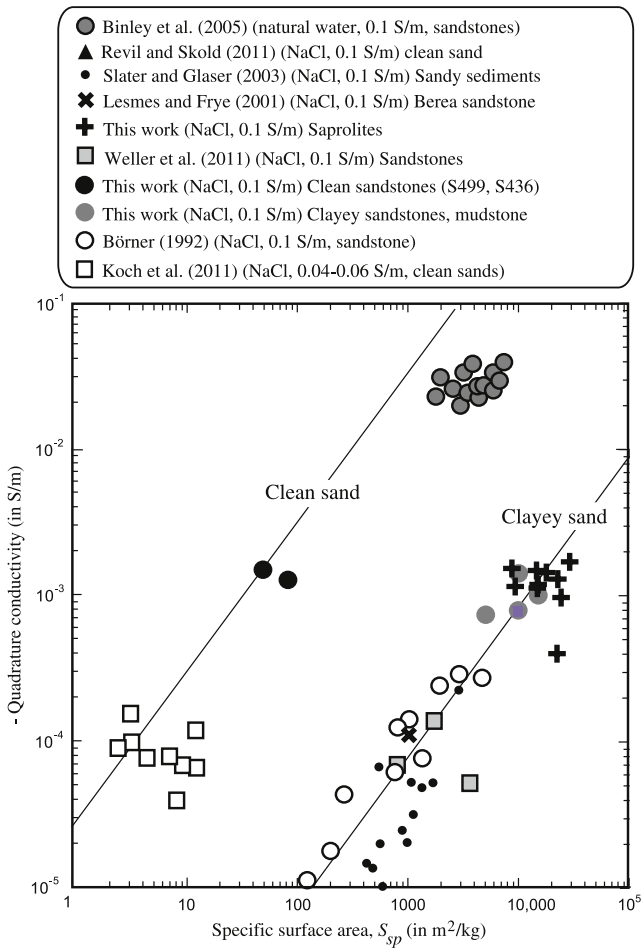

Fig. 10. Influence of the specific surface area S_{Sp} upon the quadrature conductivity. Trend determined for clayey sands from the model developed by Revil [12] at 0.1 S m^{-1} NaCl. For the data from [13] and [55–59], the measurements are reported at 10 Hz. For the data from Binley et al. [60] (Eggborough and Hatfield sandstones), they are reported at 1.4 Hz.

one for clayey materials. This indicates that the mobilities of the counterions in the Stern layer of silicates and aluminosilicates are very different from each other.

5.3. Dependence on the salinity

In Figs. 11 and 12, we test the dependence of the phase and quadrature conductivity on the pore water conductivity. In Fig. 10, we test Eq. (19) together with the data on the saprolite core samples using $\beta^S_{(+)}$ (Na$^+$) = 1.5 × 10^{-10} m^2 s^{-1} V^{-1} and $B_{(+)}$ (Na$^+$) = 5.6 × 10^{-8} m^2 s^{-1} V^{-1} at 25 °C (see Section 2). The data are fitted with a constant value of the partition coefficient f = 0.92 and a charge per unit volume of 5.7 × 10^7 C m^3 as determined in Fig. 11. The partition coefficient is consistent with the presence of illite in the pore space, while the charge per unit pore volume is consistent with Eq. (20). Indeed, taking a grain density of ρ_g of 2650 kg m^{-3}, a cation exchange capacity CEC of 6 cmol kg^{-1} (see Table 2) and a porosity of φ = 0.40 (Table 1), we obtain Q_V = 2.3 × 10^7 C m^{-3}.

In Fig. 12, we test the prediction of Eq. (39) regarding the salinity dependence of the quadrature conductivity with the pore water conductivity. Eq. (39) is able to represent all the saprolite data fairly well. Using taking CEC$_M$ = 6 × 10^3 C kg^{-1} (see Table 2), $\beta^S_{(+)}$ (25 °C, Na$^+$) = 1.5 × 10^{-10} m^2 s^{-1} V^{-1} (see Section 5.2), and f_M = 0.92 (high salinity asymptotic value) yields σ''_M = −(1.1–1.9) × 10^{-3} S m^{-1} at high salinities in excellent agreement with the laboratory data shown in Fig. 12 (see the high salinity asymptote for which σ''_M = −(1.5) × 10^{-3} S m^{-1}).

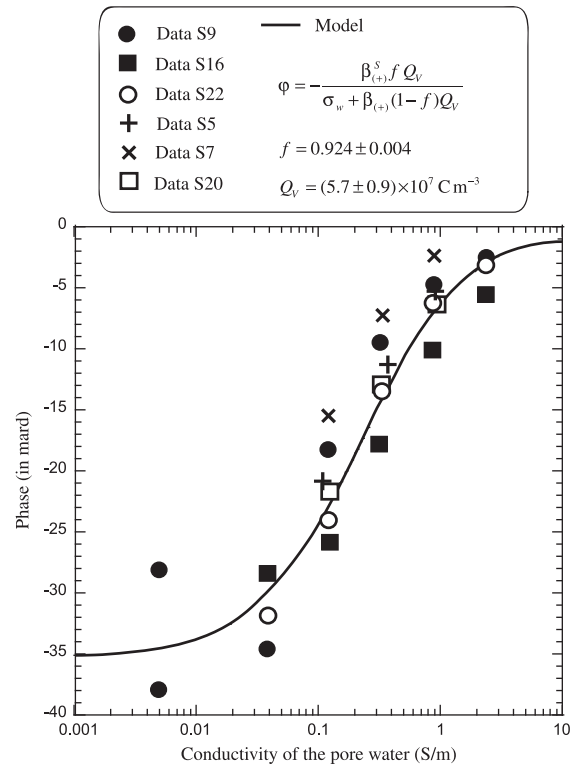

Fig. 11. Determination of the partition coefficient f (fraction of the counterions in the Stern layer) and total volumetric charge density Q_V using the phase lag data plotted as a function of the conductivity of the pore water (at 1 Hz, NaCl). The plain line corresponds to the best fit of the model using a constant value of the partition coefficient.

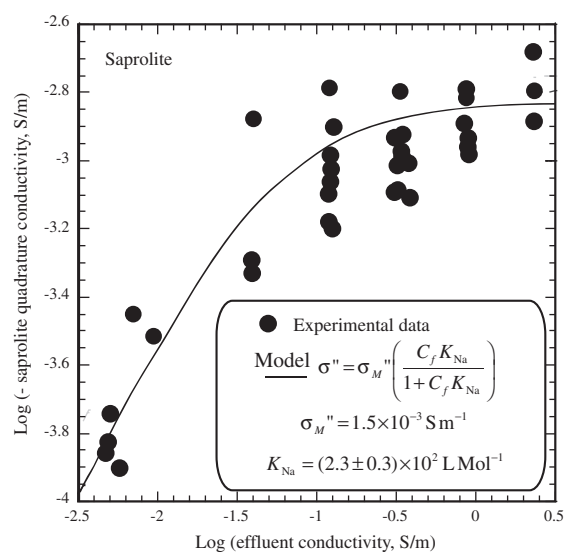

Fig. 12. Dependence of the quadrature conductivity with the salinity (all the saprolite core samples, NaCl, pH ~ 5–6). The plain line corresponds to the prediction of the model. Note that the quadrature conductivity data reach a plateau at high salinities.

5.4. Dependence on frequency

We develop a methodology to invert the Cole–Cole parameters using the genetic algorithm. We first determined the initial values of the Cole–Cole parameters with the use of two existing deterministic algorithms from [50,51]. An extensive series of tests of these two algorithms showed that there were not able to converge property in fitting our data (not shown here). That

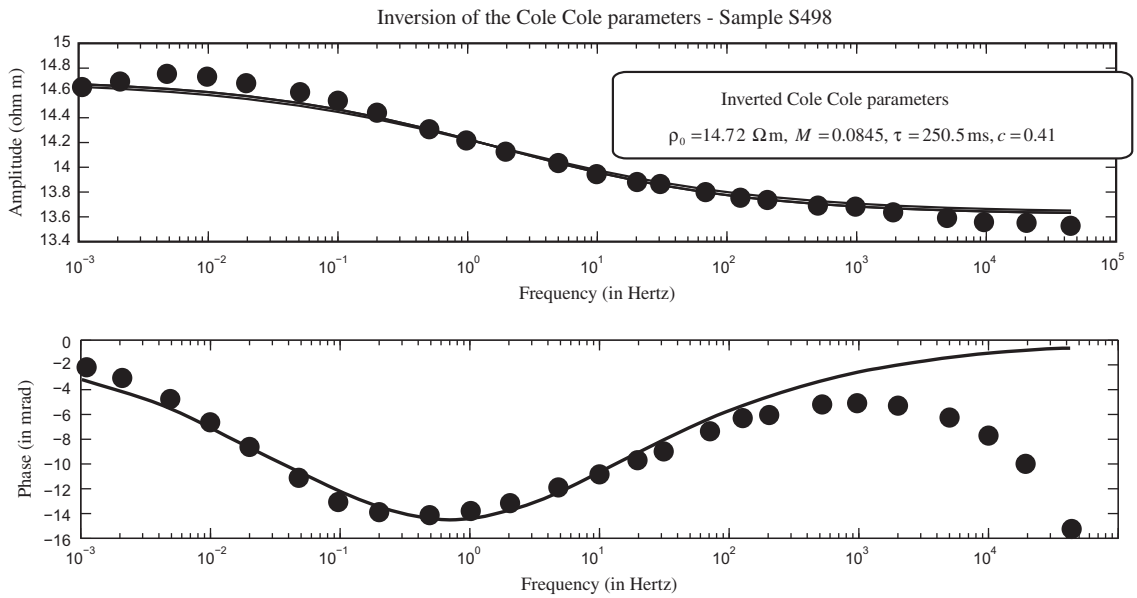

Fig. 13. Inversion of the Cole–Cole parameters using the genetic algorithm. Example for Sample S498. The filled circles correspond to the measurements for the amplitude of the resistivity and the phase. Above 100 Hz, the measurements are not considered very reliable and so we did not try to match the data above 1 kHz.

said, if we used these algorithms to get a set of values for the Cole–Cole parameters, which are then used as starting parameters for the genetic algorithm, we obtain an excellent fit of the data (Fig. 13). The genetic algorithm we used is based on the built-in MATLAB Global Optimization Toolbox.

In Fig. 14a, we show that the Cole–Cole time constant inverted from the genetic algorithm seems independent on the salinity of the pore water solution. This is consistent with our model as the diffusion coefficient of the counterions in the Stern layer is expected to have only a weak dependence on the salinity. We have performed a similar analysis for the Cole–Cole exponent (Fig. 14b), and we found also that the Cole–Cole exponent c is independent on the salinity of the pore water.

5.5. Dependence on the pore size

We are now in the position to determine the relationship between the Cole–Cole time constant and the pore size. If we look at Fig. 3, we see that Samples S490, S499, and S436 are characterized by the biggest pores (median in the range 12–14 μm). Their spectra peak at low frequencies (0.05–0.1 Hz, see Fig. 4). At the opposite, Sample S439 is characterized by narrow pores (median 0.5 μm), and its phase peaks at high frequencies (10 Hz).

In Figs. 15 and 16, we plot the Cole–Cole time constant versus the pore size of the material, either determine from the permeability or from mercury intrusion experiments. In the first case, the permeability is related to the mean pore size by,

$$k = \frac{\Lambda^2}{8F}. \tag{50}$$

where F denotes the formation factor discussed in Appendix A. Katz and Thompson [52] developed a relationship between the permeability and a percolation length scale R_c that can be determined from mercury data: $k_S = R_c^2/(226F)$. A comparison between this equation and Eq. (50) yields $R_c \approx 5.3\Lambda$.

We found, here again, that the data for clean sands and clayey materials split into two distinct linear trends. This observation is again consistent with a mobility of the counterions of the Stern layer of clays two orders of magnitude smaller for clays than on the surface of silica. The diffusion coefficient entering into the

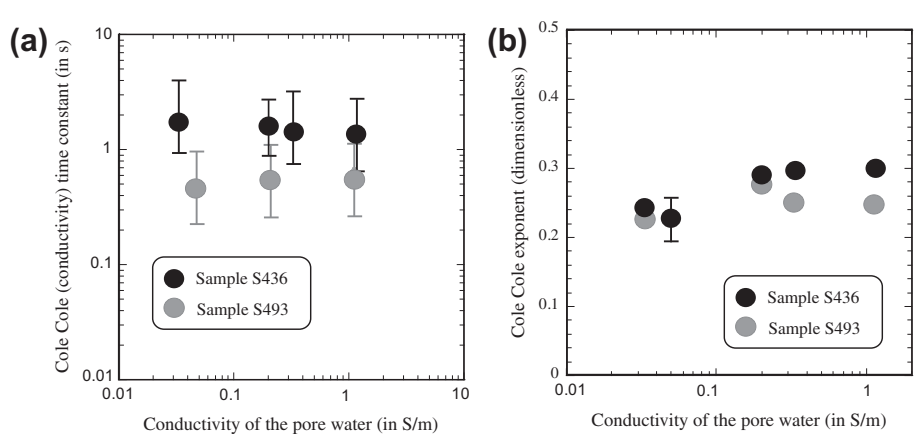

Fig. 14. Variation of the Cole–Cole time constant and the Cole–Cole exponent for two sandstone core samples as a function of the pore water conductivity. (a) The Cole–Cole time constants were determined from the spectra using the genetic algorithm as explained in the main text. The samples are chosen to represent the full range of grain sizes (sample S436 is the coarsest oxidized sandstone, sample S493 is a reduced medium to fine grained silty sandstone). The trends shown by the data are inside the error bars of the inverted Cole–Cole time constant. (b) The Cole–Cole exponent versus the pore water conductivity for the same samples. The error bar is typical of the Cole–Cole exponent estimates.

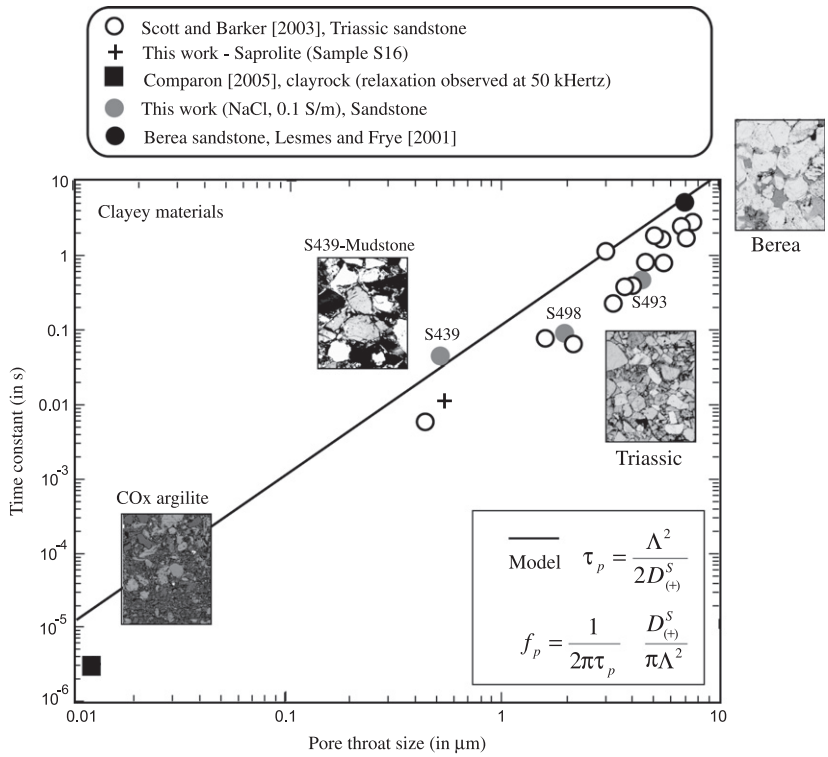

Fig. 15. Relationship between the low-frequency time constant and the mean size of the pore throat for clayey materials. The size of the thin section images is 1 mm in *x*. COx stands for Callovo–Oxfordian. The plain line corresponds to the prediction of the model. Data from [59,61,62].

expression of the Cole–Cole time constant is indeed related to the mobility of the counterions in the Stern layer, $\beta^S_{(+)}$, by the Nernst–Einstein relationship,

$$D^S_{(+)} = \frac{k_b T}{|q_{(+)}|}\beta^S_{(+)}, \tag{51}$$

where $|q_{(+)}|$ is the absolute value of the charge of the counterions in the Stern layer. A value of $\beta^S_{(+)}$ (Na^+, 25 °C) = 1.5×10^{-10} $m^2\ s^{-1}\ V^{-1}$ (Section 5.3) yields $D^S_{(+)}$ (Na^+, 25 °C) = 3.8×10^{-12} $m^2\ s^{-1}$ for clays. This value is used to compute the trends for clayey materials shown in Figs. 15 and 16. For the clean sands and sandstones, we use the value of the mobility of the cations in water, which leads to a diffusion coefficient of $D^S_{(+)}$ (Na^+, 25 °C) = 1.32×10^{-9} $m^2\ s^{-1}$.

Another point worth discussion is the relationship between the value of the Cole–Cole exponent *c* and the broadness of the distribution of the pore sizes (see Fig. 3). Samples S490 and S499 have a relatively high value of *c* (0.4–0.5) and are characterized by narrow peaks in the pore size distribution (Fig. 3). At the opposite, Samples S493 and S439 have low value of *c* (flatter spectra) and are also characterized by broader distributions of their pore sizes. So, the value of *c* could be associated with the broadness of the pore size distribution with values close to 0 for very broad pore size distributions and close to 0.5 for very narrow pore size distributions.

In Table 4, we report the value of the Cole–Cole exponent *c*, the value of the cementation exponent *m*, and the broadness of the pore size distribution. We see that the Cole–Cole exponent is always comprised between 0.5 (in this case, the Cole–Cole model is equal to a Warburg impedance model) to values smaller than 0.10 (very flat spectra). The cementation exponent *m* is always larger or equal to unity (Appendix A).

We plot these data in Fig. 17 using a rough marker of the grain size distribution (very sharp, sharp, broad, and very broad). Domain A is characterized by very narrow pore size distributions and cementation exponent close to 1.5, which is the theoretical value according to the differential effective medium theory for a pack of spherical grains. The value of the Cole–Cole exponent for this domain is the one corresponding to a Warburg impedance. This is typically the domain corresponding to clean well-sorted sands. Domain B is characterized by complex microgeometry, broad pore

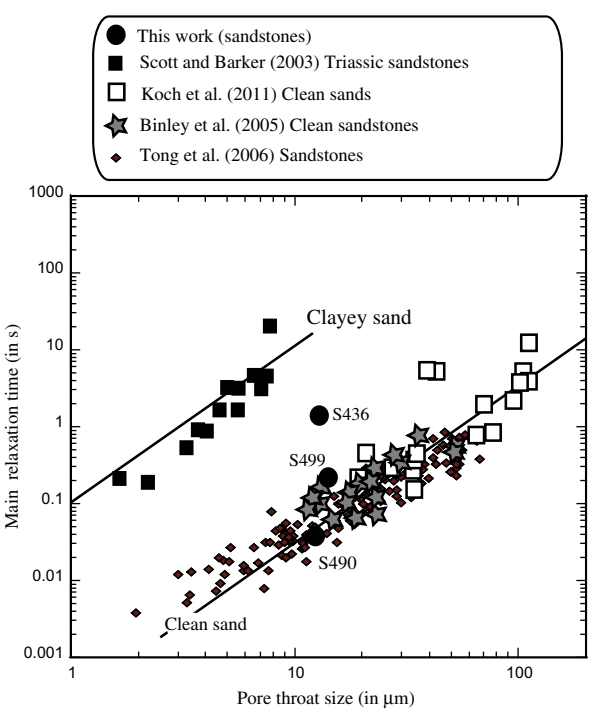

Fig. 16. Main relaxation time τ_0 versus the pore size Λ. The pore size data from this study are median values obtained from mercury injection data or permeability data. For the data from [55], the pore size is determined from the median grain size and the formation factor using the relationship developed by Revil and Florsch [10]. The mean pore size is either determined from mercury intrusion porosimetry [60] or from permeability for the data of Tong et al. [63]). The plain lines correspond to the prediction of the model.

Table 4
Relationship between the sharpness of the pore size distribution and the value of the Cole–Cole exponent *c*.

Sample	Refs.	Sharpness	*c*	*m*
S499	This work	Sharp	0.41	1.30
S498	This work	Sharp	0.37	1.39
S490	This work	Sharp	0.28	1.71
S493	This work	Very broad	0.23	1.99
S439	This work	Very broad	0.23	1.65
S436	This work	Broad	0.23	1.50
S9	This work	Very broad	0.15	1.92
S22	This work	Very broad	0.09	1.81
A1	[53]	Very sharp	0.56	1.32
F36	[54]	Sharp	0.47	1.59
F32	[54]	Sharp	0.58	1.54
WQ1	[54]	Sharp	0.32	1.56
SP1	[54]	Very sharp	0.57	1.48
SP2	[54]	Very sharp	0.32	1.49
SP3	[54]	Very sharp	0.47	1.65
SP4	[54]	Very sharp	0.37	1.58
SP5	[54]	Very sharp	0.33	1.54
SP6	[54]	Very sharp	0.22	1.70
F36-C	[54]	Sharp	0.32	1.48
F32-C	[54]	Sharp	0.35	1.40
WQ1-C	[54]	Sharp	0.44	1.59
SP1-C	[54]	Very sharp	0.50	1.30
SP2-C	[54]	Very sharp	0.40	1.35
SP3-C	[54]	Very sharp	0.45	1.49
SP4-C	[54]	Very sharp	0.28	1.54
SP5-C	[54]	Very sharp	0.33	1.44
SP6-C	[54]	Very sharp	0.28	1.53

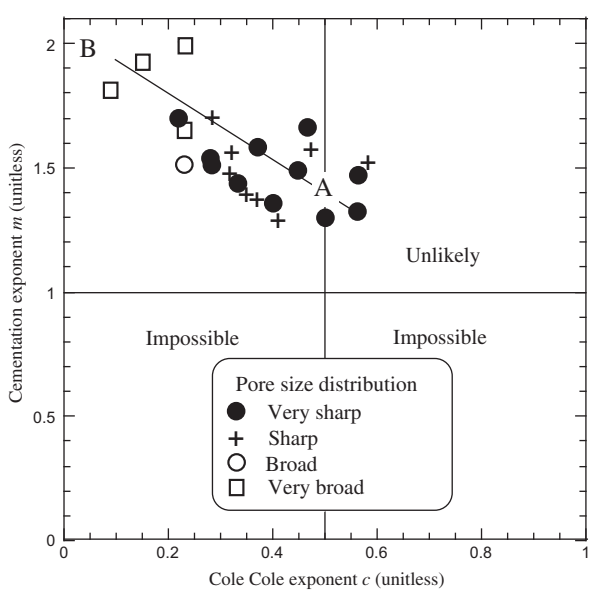

Fig. 17. Cementation exponent *m* versus the Cole–Cole exponent *c*. There are two extreme end-regions denoted as A and B. Domain A is typical of well-sorted clean sands while domain B is typical of clay-rich materials. The plain line denotes the trend between *m* and *c*.

size distributions, and the presence of clays. For this domain, the Cole–Cole exponent reaches small values consistent with the broad pore size distributions, and *m* reaches a value close to 2 characterizing a complex pore space topology. This implies that the exponent *c* is a measure of the pore size distribution and that for a pore distribution defined by the delta function, the frequency-dependent model is the Warburg model. This also implies that the Debye decomposition used in various disciplines (colloidal chemistry and geophysics for instance) to determine the distribution of relaxation times is not correct (it would imply indeed that

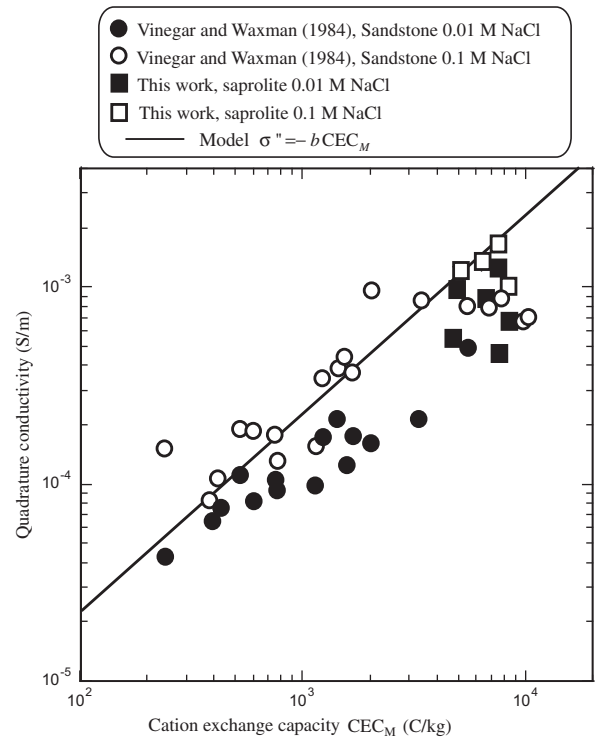

Fig. 18. Quadrature conductivity versus the cation exchange capacity at different salinities (0.01 and 0.1 M NaCl). The line represents the prediction of our model as discussed in the main text. The data shows clearly the effect of salinity on the quadrature conductivity.

if all the pores are the same, the Cole–Cole exponent should be equal to 1, which translates to a Debye model). In other words, complex conductivity spectra should be deconvoluted by a Warburg model to obtain the pore size distribution. Such pore size distribution could be compared to the T2 relaxation time distributions from nuclear magnetic resonance (NMR) spectra. We let this point for a future work.

5.6. Dependence on the CEC

As explained in Section 4.4, the CEC and the specific surface area are related to each other by $Q_S = \mathrm{CEC}_M/S_{sp}$ where the surface charge density Q_S is about 0.32 C m^{-2}. Using this relationship in Eq. (36), we obtain,

$$\sigma'' = -b\mathrm{CEC}_M, \tag{52}$$

$$b = \frac{a}{Q_S} = \frac{2}{3}\beta^S_{(+)} f \rho_g. \tag{53}$$

For clayey sands, taking $a = 7.6 \times 10^{-8}$ S kg m^{-3}, we obtain $b = 2.38 \times 10^{-7}$ S kg C^{-1} m^{-1}. The prediction of Eq. (52) with $b = 2.38 \times 10^{-7}$ S kg C^{-1} m^{-1} is shown in Fig. 18 with both the experimental data of [53] and those of the present work. There is a fair agreement between the model and the data.

6. Conclusions

We have reached the following conclusions.

(1) We have developed a simple polarization model accounting for the dependence of the in-phase and quadrature conductivities on the porosity, cation exchange capacity (or specific surface area of the material), and salinity of the pore water for simple supporting electrolytes like NaCl in isothermal

conditions. This model is coupled with a very simple complexation model on the surface of the minerals. This model is used to define the salinity dependence of the partition coefficient of the counterions between the Stern and diffuse layers.

(2) The quadrature conductivity of sands and sandstones seems to be controlled by the polarization of the Stern layer. The mobility of the counterions in the Stern layer of silica sands is two orders of magnitude higher than the mobility of the counterions in the Stern layer of clay minerals. This is confirmed through the inversion of the Cole–Cole time constant as the diffusion coefficient entering this time constant can be related as well to the mobility of the counterions in the Stern layer.

(3) The salinity dependence of the in-phase and quadrature conductivity are very well-explained by our model. The quadrature component is controlled by the salinity dependence of the partition coefficient for the counterions between the Stern and diffuse layers.

(4) The frequency dependence of the complex conductivity is usually well described by a Cole–Cole model with a Cole–Cole exponent comprised between 0.5 (for very narrow pore size distribution) to values smaller than 0.10 for very broad pore size distributions. Both the Cole–Cole exponent and the Cole–Cole time constant are independent on the salinity of the pore water solutions for simple supporting electrolytes like NaCl.

Molecular dynamics simulations could be performed to see how to explain the mobility of the counterions in the Stern layer and to simulate the dynamic Stern layer in order to better understand low-frequency induced polarization in sandy and clayey materials. Such simulations could be also used to coupled diffuse and Stern layers polarizations.

Acknowledgments

We thank the Environment Remediation Science Program (ERSP), U.S. Department of Energy (DOE, Award DE-FG02-08ER646559) for funding. We thank Sophie Hancock for her help with the experimental data with the sandstones. We deeply thank Egon Zimmermann for the construction of the ZEL-SIP04-V02 impedance meter.

Appendix A. Physical description of the formation factor

The formation factor is defined by the electrical conductivity problem of a porous material when surface conductivity by be neglected. From Eq. (8), we have indeed,

$$\lim_{\mathrm{Du}=0}\left(\frac{\sigma''}{\sigma_w}\right)=\frac{1}{F}. \tag{A1}$$

In a porous material with insulating grains, the following canonical boundary value problem for the normalized electrical potential Γ for a cylindrical representative elementary volume of porous material of length L

$$\nabla^2\Gamma=0 \text{ in } V_p \tag{A2}$$

$$\hat{n}\cdot\nabla\Gamma=0 \text{ on } S \tag{A3}$$

$$\Gamma=\begin{cases} L \text{ at } z=L \\ \qquad\qquad \text{on } S \\ 0 \text{ at } z=0 \end{cases} \tag{A4}$$

where $\hat{n}$is the unit vector normal to the pore water/mineral interface S and V_p denote the pore volume [64]. The formation factor F is obtained by summing up the Joule dissipation of energy [64,65]). This yields,

$$\frac{1}{F}=\frac{1}{V}\int_{V_p}|\nabla\Gamma|^2 dV_p, \tag{A5}$$

where V is the total volume of the considered representative elementary volume. From Eq. (B5), $1/F$ can be regarded as an effective porosity [66], which is only a fraction of the total connected porosity $\phi=V_p/V$. This implies in turn,

$$\frac{1}{F}\leqslant\phi \text{ and } F\equiv\phi^{-m}\Rightarrow m\geqslant 1 \tag{A6}$$

Appendix B. Low and high-frequency conductivity

The main assumption made in our analysis is that the grains are touching each other so the diffuse layer is continuous but not the Stern layer [12]. Under this assumption, we expect that the Direct Current (DC) conductivity and the high-frequency conductivity are given by,

$$\sigma_0=\frac{1}{F}\left[\sigma_w+\beta_{(+)}(1-f)Q_V\right], \tag{B1}$$

$$\sigma_\infty=\frac{1}{F}\left\{\sigma_w+\left[\beta_{(+)}(1-f)+\beta^S_{(+)}f\right]Q_V\right\}. \tag{B2}$$

These equations can be demonstrated through a volume averaging approach [26]. The normalized chargeability $M_n=M\sigma_\infty=\sigma_\infty-\sigma_0$ is therefore, using Eq. (20), the normalized chargeability is given as,

$$M_n=\left(\frac{1}{F}\right)\left(\frac{1-\phi}{\phi}\right)\rho_g\beta^S_{(+)}f\mathrm{CEC}, \tag{B3}$$

$$M_n\approx\left(\frac{2}{3}\right)\rho_g\beta^S_{(+)}f\mathrm{CEC}, \tag{B4}$$

which is also the same equation obtained for the quadrature conductivity (see Eq. (36)). To go from Eq. (B3) to Eq. (B4), we have used the approximations (see [10]),

$$F-1\approx F, \tag{B5}$$

$$F\approx 1+\frac{3}{2}\left(\frac{\phi}{1-\phi}\right). \tag{B6}$$

References

[1] L. Onsager, Phys. Rev. 37 (1931) 405–426.
[2] I. Prigogine, Etude Thermodynamique des Phénomènes Irréversibles, Desoer, Liège, Belgium, 1947.
[3] A. Revil, N. Linde, J. Colloid Interface Sci. 302 (2006) 682–694.
[4] C. Grosse, J. Phys. Chem. B 115 (29) (2011) 8996–9004.
[5] P. Leroy, A. Revil, A. Kemna, P. Cosenza, A. Ghorbani, J. Colloid Interface Sci. 321 (1) (2008) 103–117.
[6] I.A. Razilov, S.S. Dukhin, Colloid J. 57 (3) (1995) 364–371 [translated from Kolloidnyi Zhurnal 57(3) (1995) 391–399].
[7] S.S. Dukhin, V.N. Shilov, Dielectric phenomena and the double layer in disperse systems and polyelectrolytes, Wiley, New York, 1974.
[8] L.A. Rosen, Langmuir 7 (1991) 36–42.
[9] J. Lyklema, A.V. Delgado, Surfact. Sci. Ser. 106 (2002) 87–97. 991.
[10] A. Revil, N. Florsch, Geophys. J. Int. 181 (2010) 1480–1498, http://dx.doi.org/10.1111/j.1365-246X.2010.04573.x.
[11] M. Schmutz, A. Revil, P. Vaudelet, M. Batzle, P. Femenía Viñao, D.D. Werkema, Geophys. J. Int. 183 (2010) 211–224, http://dx.doi.org/10.1111/j.1365-246X.2010.04751.x.
[12] A. Revil, Water Resour. Res. 48 (2012), http://dx.doi.org/10.1029/2011WR011260. W02517.
[13] A. Revil, K. Koch, K. Holliger, Water Resour. Res. 48 (2012), http://dx.doi.org/10.1029/2011WR011561. W05602.
[14] A. Revil, M. Skold, S.S. Hubbard, Y. Wu, D. Watson, M. Karaoulis, Geophysics 78 (1) (2013) D21–D40, http://dx.doi.org/10.1190/geo2012-0176.1.
[15] S. Pride, Phys. Rev. B 50 (21) (1994) 15678–15696.

[16] M.J. Aranda-Rascón, C. Grosse, J.J. López-García, J. Horno, J. Colloid Interface Sci. 336 (2009) 857–864.
[17] F. Carrique, F.J. Arroyo, M.L. Jiménez, A.V. Delgado, J. Chem. Phys. 118 (4) (2003) 1945.
[18] A. Revil, P.W.J. Glover, Phys. Rev. B55 (3) (1997) 1757–1773.
[19] C.F. Zukoski, D.A. Saville, J. Colloid Interface Sci. 114 (1) (1986) 32–44.
[20] C.F. Zukoski, D.A. Saville, J. Colloid Interface Sci. 114 (1) (1986) 45–53.
[21] R. Barchini, D.A. Saville, J. Colloid Interface Sci. 173 (1995) 86–91.
[22] M. Wang, J. Liu, S. Chen, Mol. Simul. 33 (15) (2007) 1273–1277.
[23] C. Tournassat, Y. Chapron, P. Leroy, M. Bizi, F. Boulahya, J. Colloid Interface Sci. 339 (2) (2009) 533–541.
[24] S. Carroll, R.S. Maxwell, W. Bourcer, S. Martin, S. Hulsey, Geochim. Cosmochim. Acta 66 (6) (2002) 913–926.
[25] L.A. Rosen, J.C. Baygents, D.A. Saville, J. Chem. Phys. 98 (5) (1993) 4183–4194.
[26] A. Revil, Water Resour. Res. 49 (2013) doi:10.1029/2012WR012700.
[27] G.E. Archie, Trans. AIME 146 (1942) 54–62.
[28] K.S. Cole, R.H. Cole, J. Chem. Phys. 9 (1941) 341–351.
[29] D.B. Watson, J.E. Kostka, M.W. Fields, P.M. Jardine, NABIR FRC Technical Report: NABIR FRC, 2004. <http://public.ornl.gov/orifc/FRC-conceptual-model.pdf>.
[30] P.M. Jardine, G.V. Wilson, R.J. Luxmoore, Soil Sci. Soc. Am. J. 52 (1988) 1252–1259.
[31] P.M. Jardine, G.K. Jacobs, G.V. Wilson, Soil Sci. Soc. Am. J. 57 (1993) 945–953.
[32] P.M. Jardine, G.K. Jacobs, J.D. O'Dell, Soil Sci. Soc. Am. J. 57 (1993) 954–962.
[33] Y.J. Kim, J.W. Moon, Y. Roh, S.C. Brooks, Environ. Geol. 58 (2009) 1301–1307.
[34] E. Zimmermann, A. Kemna, J. Berwix, W. Glaas, H.M. Münch, J.A. Huisman, Meas. Sci. Technol. 19 (2008), http://dx.doi.org/10.1088/0957-0233/19/10/105603.
[35] A. Revil, M. Skold, Geophys. J. Int. 187 (2011) 813–824, http://dx.doi.org/10.1111/j.1365-246X.2011.05181.x.
[36] B.F. Swanson, J. Petrol. Technol. 33 (1981) 2498–2504.
[37] M.E. Sumner, W.P. Miller, Cation exchange capacity and exchange coefficients, in: D.L. Page (Ed.), Methods of Soil Analysis Part 3: Chemical Methods, Soil Science Society of America, Madison, WI, 1996.
[38] K.S.W. Sing, Pure Appl. Chem. 57 (4) (1985) 603–619.
[39] S. Brunauer, P.H. Emmett, E. Teller, J. Am. Chem. Soc. 60 (1938) 309–319.
[40] A. Revil, L.M. Cathles, S. Losh, J.A. Nunn, J. Geophys. Res. 103 (B10) (1998) 23,925–23,936.
[41] J.G. Patchett, Society of Professional Well Logging Analysis 16th Logging Symposium, Paper U, 1975, p. 41.
[42] M. Lipsicas, Physics and chemistry of porous media, in: D.L. Johnson, P.N. Sen (Eds.), Am. Inst. of Phys., College Park, Md., 1984, pp. 191–202.
[43] J.P. Zundel, B. Siffert, in: Solid–Liquid Interactions in Porous Media, Technip, Paris, 1985, pp. 447–462.
[44] N.C. Lockhart, J. Colloid Interface Sci. 74 (1980) 520–529;
V.A. Sinitsyn, S.U. Aja, D.A. Kulik, S.A. Wood, Geochim. Cosmochim. Acta 64 (2000) 185–194.
[45] M.J. Avena, C.P. De Pauli, J. Colloid Interface Sci. 202 (1998) 195–204, http://dx.doi.org/10.1006/jcis.1998.5402.
[46] I. Shainberg, N. Alperovitch, R. Keren, Clays Clay Miner. 36 (1988) 432–438.
[47] Q. Su, Q. Feng, Z. Shang, Geophysics 65 (2000) 68–75.
[48] C. Ma, R.A. Eggleton, Clays Clay Miner. 47 (1999) 174–180.
[49] B. Chittoori, A.J. Puppala, J. Geotech. Geoenviron. Eng. 137 (11) (2011) 997–1008.
[50] A. Kemna, Tomographic Inversion of Complex Resistivity-Theory and Application, Ph.D. Dissertation, Ruhr-University of Bochum, Germany, 2000, 196pp.
[51] J. Xiang, D. Cheng, F.S. Schlindwein, N.B. Jones, Comput. Geosci. 29 (2003) 647–654.
[52] A.J. Katz, A.H. Thompson, J. Geophys. Res. 92 (1987) 599–607.
[53] H.J. Vinegar, M.H. Waxman, Geophysics 49 (1984) 1267–1287.
[54] P. Vaudelet, A. Revil, M. Schmutz, M. Franceschi, P. Bégassat, Water Resour. Res. 47 (2011) W02526, http://dx.doi.org/10.1029/2010WR009310.
[55] K. Koch, A. Kemna, J. Irving, K. Holliger, Hydrol. Earth Syst. Sci. 15 (2011) 1785–1794, http://dx.doi.org/10.5194/hess-15-1785-2011.
[56] L.D. Slater, D.R. Glaser, Geophysics 68 (5) (2003) 1547–1558.
[57] A. Weller, K. Breede, L. Slater, S. Nordsiek, Geophysics 75 (6) (2011) F315–F327.
[58] F.D. Börner, Proc. Third European Core Analysis Symposium, Paris, 1992, pp. 359–386.
[59] D.P. Lesmes, K.M. Frye, J. Geophys. Res. 106 (B3) (2001) 4079–4090.
[60] A. Binley, L.D. Slater, M. Fukes, G. Cassiani, Water Resour Res. 41 (2005) W12417.
[61] J. Scott, R. Barker, Geophys. Res. Lett. 30 (9) (2003) 1450.
[62] L. Comparon, Etude expérimentale des propriétés électriques et diélectriques des matérieux argileux consolidés, PhD Thesis, Institut de Physique du Globe de Paris, 2005, 400pp.
[63] M. Tong, L. Li, W. Wang, Y. Jiang, Geophysics 71 (2006) N33–N40.
[64] D.L. Johnson, T.J. Plona, H. Kojima, in: R. Jayanth, J. Banavar, K.W. Winkler (Eds.), Physics and Chemistry of Porous Media II, AIP, New York, 1986, pp. 243–277.
[65] M. Avellaneda, S. Torquato, Phys. Fluids A 3 (1991) 2529–2540.
[66] A. Revil, L.M. Cathles III, Water Resour. Res. 35 (1999) 651–662.